Targeting parvalbumin-expressing neurons in the substantia nigra pars reticulata restores motor function in parkinsonian mice

Lorena Delgado-Zabalza, Nicolas Mallet, Christelle Glangetas, Guillaume Dabee, Maurice Garret, Cristina Miguelez, Jérôme Baufreton

Cell Reports

Article

Targeting parvalbumin-expressing neurons in the substantia nigra pars reticulata restores motor function in parkinsonian mice

Graphical abstract

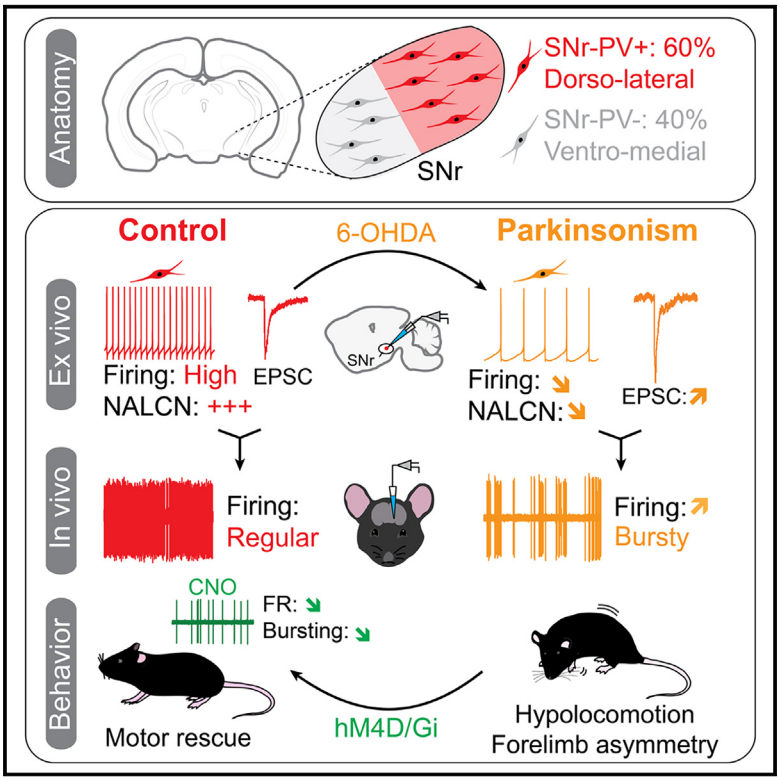

Highlights

- SNr-PV+ neurons have distinctive anatomical and electrophysiological signatures
- NALCN channels are downregulated in SNr-PV+ neurons from PD mice
- SNr-PV+ cells *in vivo* show altered firing pattern underlying motor symptoms in PD
- Chemogenetic manipulation of SNr-PV+ neurons restores motor control in PD mice

Authors

Lorena Delgado-Zabalza, Nicolas Mallet, Christelle Glangetas, Guillaume Dabee, Maurice Garret, Cristina Miguelez, Jérôme Baufreton

Correspondence

jerome.baufreton@u-bordeaux.fr

In brief

Delgado-Zabalza et al. show that downregulation of NALCN channels underlies *ex vivo* hypoexcitability and *in vivo* altered firing pattern of SNr-PV+ in experimental parkinsonism. Chemogenetic manipulation of SNr-PV+ neurons is sufficient to restore motor function in parkinsonian mice, demonstrating the key role of this cell type in motor control.

Delgado-Zabalza et al., 2023, Cell Reports ■■, 113287
■■, 2023
https://doi.org/10.1016/j.celrep.2023.113287

CellPress

Please cite this article in press as: Delgado-Zabalza et al., Targeting parvalbumin-expressing neurons in the substantia nigra pars reticulata restores motor function in parkinsonian mice, Cell Reports (2023), https://doi.org/10.1016/j.celrep.2023.113287

Cell Reports

CellPress
OPEN ACCESS

Article

Targeting parvalbumin-expressing neurons in the substantia nigra pars reticulata restores motor function in parkinsonian mice

Lorena Delgado-Zabalza,[1,2] Nicolas Mallet,[1] Christelle Glangetas,[1] Guillaume Dabee,[1] Maurice Garret,[3] Cristina Miguelez,[2,4] and Jérôme Baufreton[1,5,*]

[1]University Bordeaux, CNRS, IMN, UMR 5293, 33000 Bordeaux, France
[2]Department of Pharmacology. University of the Basque Country (UPV/EHU), 48940 Leioa, Spain
[3]University Bordeaux, CNRS, INCIA, UMR 5287, 33000 Bordeaux, France
[4]Autonomic and Movement Disorders Unit, Neurodegenerative Diseases, Biocruces Health Research Institute, Barakaldo, Spain
[5]Lead contact
*Correspondence: jerome.baufreton@u-bordeaux.fr
https://doi.org/10.1016/j.celrep.2023.113287

SUMMARY

The activity of substantia nigra pars reticulata (SNr) neurons, the main output structure of basal ganglia, is altered in Parkinson's disease (PD). However, neither the underlying mechanisms nor the type of neurons responsible for PD-related motor dysfunctions have been elucidated yet. Here, we show that parvalbumin-expressing SNr neurons (SNr-PV+) occupy dorsolateral parts and possess specific electrophysiological properties compared with other SNr cells. We also report that only SNr-PV+ neurons' intrinsic excitability is reduced by downregulation of sodium leak channels in a PD mouse model. Interestingly, in anesthetized parkinsonian mice *in vivo*, SNr-PV+ neurons display a bursty pattern of activity dependent on glutamatergic tone. Finally, we demonstrate that chemogenetic inhibition of SNr-PV+ neurons is sufficient to alleviate motor impairments in parkinsonian mice. Overall, our findings establish cell-type-specific dysfunction in experimental parkinsonism in the SNr and provide a potential cellular therapeutic target to alleviate motor symptoms in PD.

INTRODUCTION

The basal ganglia (BG) are a group of interconnected subcortical nuclei that broadcast cortical motor commands to the diencephalon and brainstem circuits for proper control of actions selection and execution. The loss of midbrain dopaminergic neurons as in Parkinson's disease (PD) disrupt BG neuronal activity and network communication, leading to profound motor impairments such as bradykinesia, akinesia, and locomotor deficits. However, the cellular mechanisms underlying such change in activity and its link with motor dysfunction, especially at the output level of BG circuits, remain largely unknown.

The substantia nigra pars reticulata (SNr) is the main output nucleus of rodents BG and serves as an inhibitory gate over motor output[1] via its projections to the motor thalamus and the brainstem.[2] The SNr is composed of several neuronal subpopulations according to their molecular signature or phenotype[3–6] or their projection targets.[7,8] All SNr neurons display regular pacemaking firing activity *ex vivo*,[9–12] but exhibit complex movement-related non-correlated neuronal activity patterns during motor behavior and brain state changes.[13–16] It has been recently proposed that sleep-wake transition and motor behaviors are controlled by distinct SNr neuronal populations, namely glutamic acid decarboxylase 2-expressing SNr neurons (SNr-GAD2+) and parvalbumin-expressing SNr (SNr-PV+) neurons, respectively,[16] suggesting that motor control is supported by SNr-PV+ cells.

According to the original rate model of the BG,[17,18] the output neurons of the BG are hyperactive in PD. This statement remains debated as some studies report either an increase,[19] a decrease,[20,21] or no change[22–24] in the firing activity of SNr neurons. In addition, it is well established that SNr neurons fire more irregularly and synchronously in experimental models of PD[19,23–27] compared with normal condition. However, a comprehensive understanding of the contribution of specific subpopulations of SNr neurons, and in particular motor-related PV+ neurons, in the pathophysiology of PD is still lacking.

In this study, we investigated the consequences of dopamine depletion on the excitability of SNr neurons using a mouse model of PD. We observed that SNr-PV+ neurons are distributed in the dorso-lateral portion of the SNr corresponding with the motor domain of the nucleus. Furthermore, we identified that the pacemaking activity of SNr-PV+ neurons *ex vivo* is reduced in parkinsonian mice because of the downregulation of sodium leak channels (NALCNs) and contribute to pathological bursting activity of this cell type *in vivo* in dopamine-depleted mice. We finally demonstrated that selective chemogenetic inhibition of SNr-PV+ neurons is sufficient to alleviate motor dysfunctions in a parkinsonian state.

Please cite this article in press as: Delgado-Zabalza et al., Targeting parvalbumin-expressing neurons in the substantia nigra pars reticulata restores motor function in parkinsonian mice, Cell Reports (2023), https://doi.org/10.1016/j.celrep.2023.113287

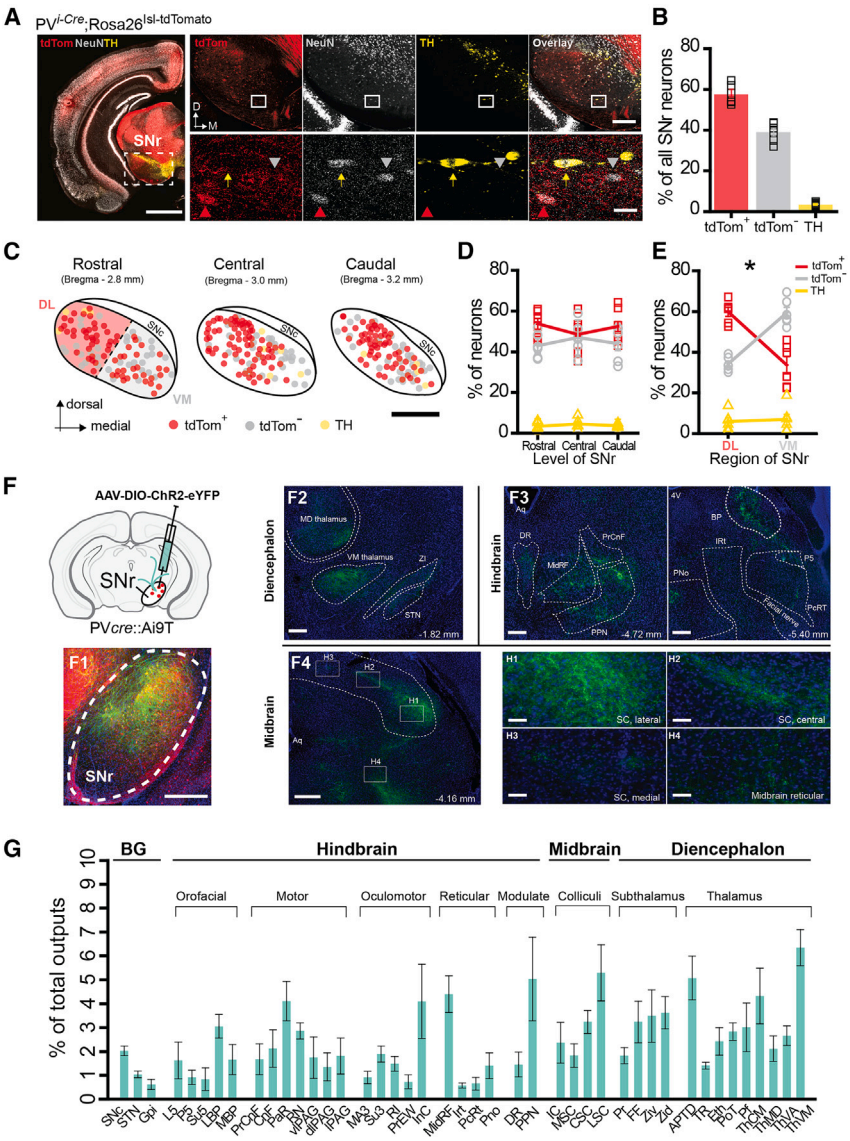

Figure 1. Immunohistochemical identification of the proportion and the distribution of SNr-PV+ neurons and their whole brain projection pattern

(A) (Left) Low-magnification images showing triple immunofluorescence labeling for the NeuN (gray), tdTomato (red), and TH (yellow) in a hemi-coronal brain section (50 μm thick) of PVcreAi9T transgenic mice. Scale bar, 1 mm. (Top right) High-magnification images of the SNr. Scale bar, 200 μm. (Bottom right) NeuN labeling allowed to identify tdTomato+/TH– (red arrowheads), tdTomato–/TH– (gray arrowhead) and tdTomato–/TH+ (yellow arrow) neurons. Scale bar, 30 μm.

(B) Quantification of the percentage of tdTomato+, tdTomato–, and TH+ SNr neurons.

(C) Distribution maps of different SNr cell types. DL, dorsolateral; VM, ventromedial. Scale bar, 500 μm.

(D) Percentage of SNr neurons at the rostral, central, and caudal levels.

(E) Quantification of SNr neurons per region.

(F) Schematic showing the injection of AAV-DIO-ChR2-eYFP in the SNr. NanoZoomer images showing transfection of SNr-PV+ neurons (F1) and the main SNr-PV+ input-recipient nuclei in the diencephalon (F2), the hindbrain (F3) and the midbrain (F4). Scale bars, 250 μm. (H1–H4) High magnification images of the superior colliculus (SC) (H1–H3) and the reticular formation (H4). Scale bars, 50 μm. Aq, ; BP, ; IRt, ; MidRF, ; PcRT, PNc, ; PNo, ; PPN, ; PrCnF, ; SC, Q14

(G) Quantification of SNr-PV+ ChR2-eYFP-positive fibers in 43 nuclei. Group data represent mean ± SEM. *$p < 0.05$, two-way ANOVA. See Tables S1 and S2 for more details, statistical information and abbreviations. See also Figure S1.

RESULTS

SNr-PV+ neurons are distributed in the dorso-lateral domain of the SNr and have wide projections to motor-related thalamic and brainstem nuclei

To examine the function of SNr-PV+ neurons in motor control in experimental parkinsonism, we first characterized the distribution of this subpopulation using PVcreAi9T reporter mice. Immunohistochemical triple labeling was performed in coronal slices from six PVcreAi9T mouse brains (Figure 1A). The neuronal nuclear marker (NeuN), the red fluorescent protein (tdTomato) and tyrosine hydroxylase (TH) were used as markers to identify distinct cell types in the SNr (Figure 1A). Among NeuN-positive SNr neurons, almost 58% were positive for tdTomato, only a small proportion (3%) co-localized with TH, and the remaining 39% were only positive for NeuN (Figure 1B). No differences were observed in the rostral, central, or caudal distributions between cell types (two-way ANOVA; interaction: $F_{(4, 30)} = 0.586$; $p = 0.675$) (Figures 1C and 1D). Closer examination of the distribution of SNr-PV+ neurons revealed a dorsolateral gradient (two-way ANOVA; interaction: $F_{(2, 20)} = 31.84$; $p < 0.0001$) (Figure 1E) of this subpopulation in agreement with previous studies in rodents and non-human primates,[7,16,28–32] corresponding with the SNr anatomical domain receiving sensorimotor striatal inputs.[4,33–35] To verify the validity of our mouse model, we also performed double immunohistochemistry against tdTomato and parvalbumin and found a degree of co-localization of approximately 76%, as in agreement with the literature[36] (Figure S1).

We then examined the projection pattern of SNr-PV+ neurons by injecting an adeno-associated virus (AAV) expressing a channelrhodopsin fused with enhanced yellow fluorescent protein (ChR2-eYFP) in a Cre-dependent manner in the SNr of three PVcreAi9T mice (Figure 1F). Consistent with previous findings, we found 43 nuclei throughout the brain enriched with SNr-PV+ axons.[8,16] Among them, motor-related nuclei, including the ventromedial motor thalamus, the superior colliculus, and the midbrain reticular nucleus, as well as the pedunculopontine nucleus or the cuneiform nucleus from the mesencephalic locomotor region (Figure 1G).

Please cite this article in press as: Delgado-Zabalza et al., Targeting parvalbumin-expressing neurons in the substantia nigra pars reticulata restores motor function in parkinsonian mice, Cell Reports (2023), https://doi.org/10.1016/j.celrep.2023.113287

CellPress
OPEN ACCESS

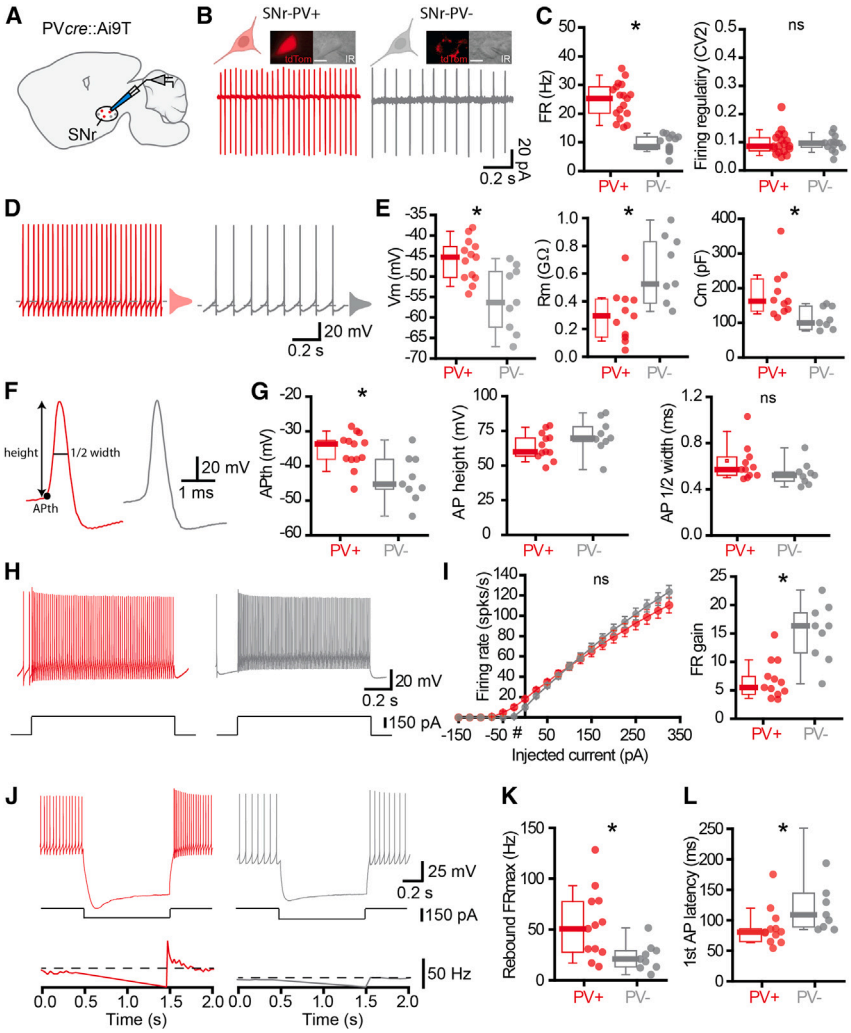

Figure 2. SNr-PV+ neurons have distinct electrophysiological properties compared with the rest of SNr neurons

(A) Diagram of the patch clamp experiment.

(B) (Top) tdTomato fluorescence (red) and DIC image (gray) showing a recorded SNr-PV+ (left) and SNr-PV– (right) neuron. Scale bar, 10 μm. (Bottom) Representative traces of cell-attached recordings from SNr-PV+ (red) and SNr-PV– (gray) neurons.

(C) Extracellular firing rates (FR) of SNr-PV+ (n = 18) and SNr-PV– (n = 14) neurons, with the corresponding CV2 graph.

(D) Representative whole cell autonomous firing (0 pA current injection) for SNr-PV+ and SNr-PV– cells.

(E) Population data depicting membrane potential (Vm), membrane input resistance (Rm), and whole-cell capacitance (Cm) (SNr-PV+, n = 12; SNr-PV–, n = 9).

(F) Average spike waveforms of SNr-PV+ and SNr-PV- neurons.

(G) Action potential (AP) properties (SNr-PV+, n = 12; SNr-PV-, n = 9).

(H) Representative traces of a SNr-PV+ and SNr-PV– neurons in response to a depolarizing current pulse (1 s; 200 pA) in current clamp.

(I) (Left) F-I relationship. (Right) Boxplot graph depicting the firing rate (FR) gain (maximal evoked frequency/spontaneous FR; SNr-PV+, n = 13; SNr-PV–; n = 9).

(J) Representative voltage responses to hyperpolarizing current injections for SNr-PV+ and SNr-PV– neurons.

(K and L) Population data showing post-inhibitory rebound frequency and rebound first AP latency (SNr-PV+, n = 12; SNr-PV–; n = 9). Box-and-whisker plots indicate medians, interquartile range, and 10%–90% ranges values. *p < 0.05. ns, not significant. See Table S2 for more details and statistical information. See also Figure S2.

SNr-PV+ neurons have different electrophysiological properties than SNr-PV– neurons

Several *ex vivo* studies have highlighted some heterogeneity in the autonomous firing activity and intrinsic properties of SNr neurons.[8,9,37] To determine whether SNr-PV+ neurons differ in their electrophysiological properties from the rest of SNr neurons, we performed *ex vivo* cell-attached and whole-cell recordings in acute brain slices (Figure 2A). SNr-PV+ neurons were targeted based on their selective tdTomato expression (Figure 2B). Both SNr-PV+ and SNr-PV– neurons were spontaneously active in cell-attached mode, with SNr-PV+ neurons firing at a higher rate compared with SNr-PV- neurons (MW-U test; $p < 0.0001$) (Figures 2B and 2C) and with a similar firing regularity (CV2; MW-U test; $p = 0.778$) (Figures 2B and 2C). Further analyses performed in whole-cell configuration also revealed differences in averaged membrane potential (Mann-Whitney *U* test; $p = 0.0148$), input resistance (MW-U test; $p = 0.005$) and membrane capacitance (Cm; Mann-Whitney *U* [MW-U] test; $p = 0.0068$; Figures 2D and 2E). We also looked at action potential properties such as the action potential threshold (MW-U test; $p = 0.0156$), the action potential height and width (MW-U test; $p > 0.05$) (Figures 2F and 2G) as well as input-output curves and firing rate gain (Figures 2H and 2I) (MW-U test; $p = 0.0004$). In addition, as described recently,[8] we found differences in post-inhibitory rebound between the two SNr subpopulations (Figure 2J). While SNr-PV+ neurons displayed a short latency and high frequency post-inhibitory rebound, PV– cells, in contrast, had a low frequency rebound (MW-U test; $p = 0.0148$) with a longer latency (MW-U test; $p = 0.0148$) (Figures 2K and 2L). It is well known that the depolarized membrane potential of SNr neurons is primarily supported by leak sodium channels,[9–12] so we hypothesized that maybe SNr-PV+ neurons possessed stronger leak sodium channels compared with SNr-PV- neurons. To test this, we performed voltage-clamp recordings of SNr-PV+ and PV– cells and we compared their holding currents depicting significant differences (Figures S2A–S2C) (MW-U test; $p = 0.043$). Bath application of tetrodotoxin (TTX, 1 μM) induced the same shift in holding current in both cell types (Figure S2D) (MW-U test; $p = 0.99$), while the substitution of extracellular sodium by N-methyl-D-glucamine (NMDG), a

Please cite this article in press as: Delgado-Zabalza et al., Targeting parvalbumin-expressing neurons in the substantia nigra pars reticulata restores motor function in parkinsonian mice, Cell Reports (2023), https://doi.org/10.1016/j.celrep.2023.113287

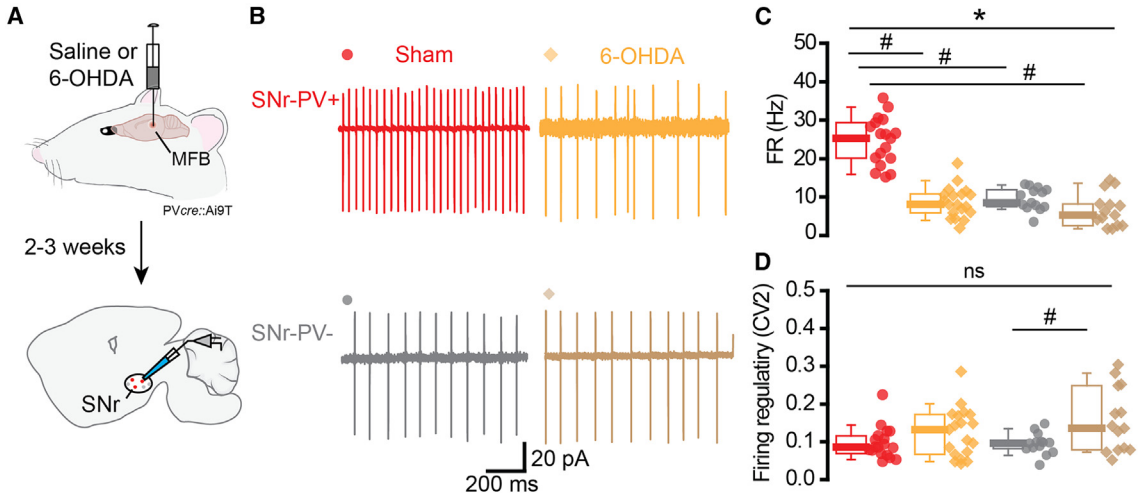

Figure 3. Dopamine-depletion selectively induces a decrease in the firing rate of SNr-PV+ neurons *ex vivo*

(A) Schematic of the experimental design to generate dopamine-depleted PVcreAi9T mice and brain slice recordings (2–3 weeks after depletion).

(B) (Top) Typical cell-attached recordings of SNr-PV+ cells from sham (red) and 6-OHDA-injected (orange) mice. (Bottom) Representative firing activity examples of SNr-PV– cells from saline (gray) and 6-OHDA (brown) injected mice.

(C) Population data showing extracellular firing rates for SNr-PV+ and SNr-PV– cells from sham (SNr-PV+; n = 18; SNr-PV–; n = 14) and 6-OHDA (SNr-PV+; n = 19; SNr-PV–; n = 14) mice. Note the significant reduction of firing rate for SNr-PV+ cells in 6-OHDA mice.

(D) Population data depicting firing regularity (CV2). Box-and-whisker plots indicate medians, interquartile range and 10%–90% ranges values. *p < 0.05, two-way ANOVA; #p < 0.05, Sidak's post hoc test. ns, not significant. See Table S2 for more details and statistical information. See also Figure S3.

large impermeant ion, generated a stronger outward shift in holding current in SNr-PV+ neurons (MW-U test; p = 0.0043) (Figure S2E).

Experimental parkinsonism selectively impacts SNr-PV+ neurons intrinsic excitability *ex vivo*

The activity of SNr neurons has been shown to be profoundly altered in experimental models of PD,[19,20,23–26,38] as well as in PD patients.[39] However, it is currently unknown if molecularly distinct SNr neurons are impacted in PD models, nor if these alterations in activity are network driven or/and caused by intrinsic excitability modifications. To address these questions, we first compared the firing rate of SNr-PV+ and SNr-PV– neurons between saline- (sham) and 6-OHDA-injected mice using *ex vivo* cell-attached recordings in acute brain slices (Figure 3A). Surprisingly, we observed a selective reduction of firing rate (two-way ANOVA, interaction: $F_{(1,\ 61)} = 31.93$; p < 0.0001) (Figures 3B–3D) only in SNr-PV+ neurons without alteration of the firing regularity (two-way ANOVA, interaction: $F_{(1,\ 61)} = 1.487$; p = 0.2274) (Figures 3B–3D). Using whole-cell recordings, we found that SNr-PV+ neurons recorded in 6-OHDA-injected mice had altered passive membrane properties as compared with SNr-PV+ neurons recorded in sham mice (Figures 4A–4F). The membrane capacitance of SNr-PV+ neurons from 6-OHDA mice was reduced compared with controls (MW-U test; p < 0.0001) (Figure 4B), suggesting a decrease in cell size after lesion that was confirmed by measuring the volume of recorded neurons (MW-U test; p = 0.0079) (Figure 4C). Their membrane resistance was also strongly increased (MW-U test; p < 0.0001) (Figure 4D) and their membrane potential more hyperpolarized (MW-U test; p < 0.0001) (Figures 4E and 4F) than SNr-PV+ neurons from sham-injected mice. The concurrent membrane hyperpolarization and increase in membrane resistance suggested the closure of a depolarizing current. We then hypothesized that 6-OHDA treatment might impact sodium leak channels function in SNr-PV+ neurons. Therefore, we performed voltage-clamp recordings and compared the holding current of SNr-PV+ clamped at −60 mV (Figures S3A–S3C) and found a significant difference between sham and 6-OHDA mice (MW-U test; *p = 0.0075) (Figure S3B). We then applied TTX (1 μM) to block voltage-dependent sodium channels (Na_V) and study sodium leak channels in isolation. Bath application of TTX produced the same shift in holding current in SNr-PV+ neurons from sham and 6-OHDA mice (MW-U test, p > 0.99) (Figure S3C), suggesting that Na_V channels function was not altered by dopamine depletion. In contrast, extracellular sodium replacement by NMDG induced a greater

shift in the holding current of SNr-PV+ neurons from sham mice compared with 6-OHDA mice (MW-U test; p = 0.0004) (Figures 4G and 4H), supporting a reduced activity of sodium leak channels in these neurons after lesion. Both transient receptor potential 3 (TRPC3) and sodium leak non-selective channels (NALCN) are expressed in SNr neurons and contribute to their depolarized potential and autonomous pacemaking properties.[10–12] To determine whether one of these two channels was dysfunctional or downregulated in SNr-PV+ neurons of 6-OHDA mice, we used the selective antagonists Pyr3 (100 μM) and L703,606 (10 μM) to inhibit TRPC3 and NALCN channels,[40] respectively. While Pyr3 had almost no effect on the holding current of SNr-PV+ neurons both in sham and 6-OHDA mice (MW-U test; p = 0.6943) (Figures 4I and 4J), L703,606 induced a strong outward shift on the holding current in SNr-PV+ neurons of sham mice, but a much moderate shift in SNr-PV+ neurons from 6-OHDA mice (MW-U test;

Please cite this article in press as: Delgado-Zabalza et al., Targeting parvalbumin-expressing neurons in the substantia nigra pars reticulata restores motor function in parkinsonian mice, Cell Reports (2023), https://doi.org/10.1016/j.celrep.2023.113287

CellPress
OPEN ACCESS

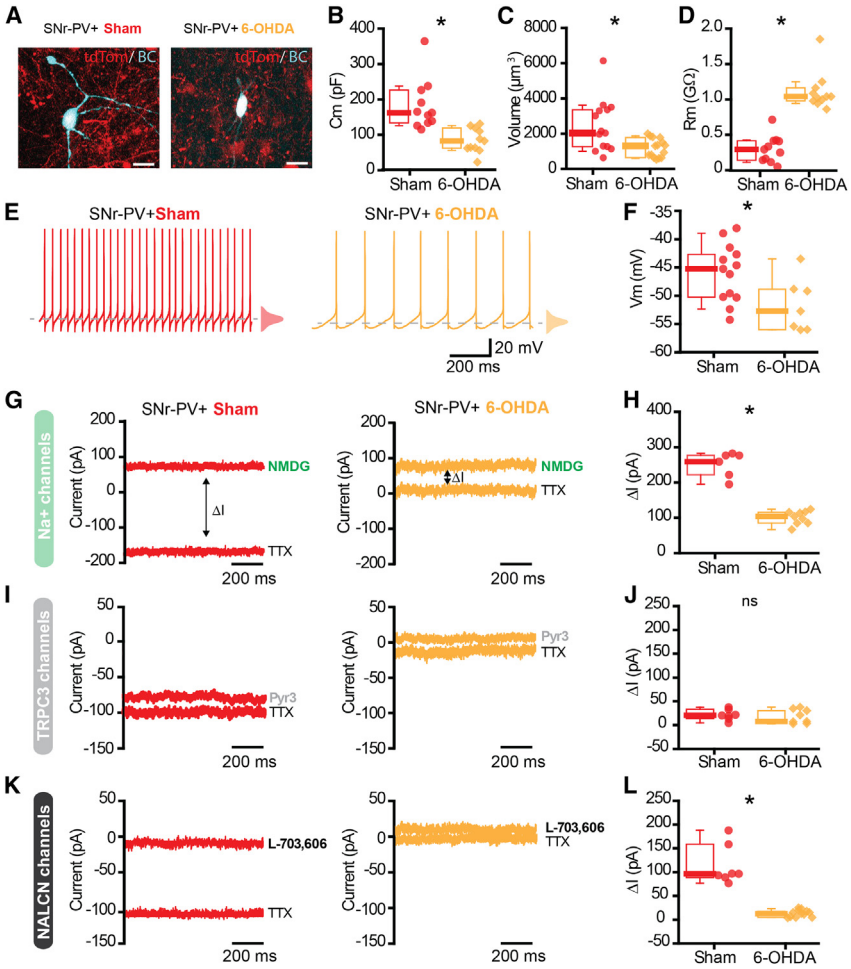

Figure 4. SNr-PV+ neurons reduced excitability is due to NALCN channels dysfunction Q15

(A) Immunofluorescence images of SNr-PV+ cells patched and filled with biocytin (BC) in sham (left) and 6-OHDA (right) mice. Scale bar, 10 µm.

(B–D) Membrane capacitance (Cm; sham, n = 11; 6-OHDA, n = 11), cell body volume (sham, n = 12; 6-OHDA, n = 16) and membrane resistance (Rm; sham n = 11; 6-OHDA n = 11) of SNr-PV+ neurons.

(E) Representative examples of SNr-PV+ neurons from sham and 6-OHDA mice recorded in current-clamp configuration.

(F) Membrane potential (Vm) observed in sham (n = 13) and 6-OHDA (n = 7) mice.

(G) Example traces of holding currents recorded in voltage-clamp mode at −60 mV in SNr-PV+ neurons from sham and 6-OHDA mice before and after Na^+ replacement with NMDG. These experiments were performed in presence of TTX (1 µM) in artificial cerebrospinal fluid.

(H) Population data from sham (n = 6) and 6-OHDA (n = 9) mice.

(I and J) Same as (G–H), but under blockade of TRPC3 channels with Pyr3 (100 µM; sham, n = 7; 6-OHDA, n = 8).

(K and L) Same as (G–H), but under pharmacological blockade of NALCN channels with L-703,606 (10 µM; sham, n = 7; 6-OHDA, n = 15). Box-and-whisker plots indicate medians, interquartile rage and 10–90 ranges values. *p < 0.05. ns, not significant; MW-U test. See Table S2 for more details and statistical information. See also Figures S3 and S4.

p > 0.0001) (Figures 4K and 4L). We also performed current-voltage recordings in control and 6-OHDA mice before and after bath application of L703,606 (10 µM) (Figures S3D and S3E). These experiments were performed in presence of ZD 7288 (10 µM) to avoid activation of hyperpolarization-activated cyclic nucleotide-gated channels. As expected, the effect of L703,606 was stronger in control mice compared with the lesioned ones throughout the voltage range tested as illustrated by the greater amplitude of L703,606-dependent current (Figures S3F–S3H) (MW-U test; p = 0.0006). Collectively, these data support a cell-specific reduction of intrinsic excitability in SNr-PV+ neurons from 6-OHDA mice caused by decreased activity of NALCN channels.

The pattern of activity of SNr-PV+ neurons is profoundly altered in parkinsonian mice *in vivo*

Increased inhibitory activity of the BG output has been suggested to be responsible for the motor symptoms in PD.[18,41,42] However, this statement remains controversial[19–24] and has never been investigated considering SNr cellular diversity. To address this issue, we performed *in vivo* extracellular recordings of SNr-PV+ neurons in sham and 6-OHDA anesthetized mice (Figure 5A). Identification of SNr-PV+ neurons was achieved using a ChR2 opto-tagging approach. This strategy relies on brief (i.e., 10-ms duration) pulses of blue light stimulation to evoke opto-spikes in SNr-PV+ cells (Figures 5B and 5C) in both sham and 6-OHDA mice. We then recorded and compared the firing rate and regularity of opto-identified SNr-PV+ neurons under similar brain state conditions (Figures 5D and 5E). Despite the apparent differences observed in the firing pattern of SNr-PV+ neurons recorded in sham vs. 6-OHDA animals (Figures 5D and 5E), the mean firing rate (MW-U test; p = 0.6877) (Figure 5F) and the firing regularity (MW-U test; p = 0.4533) (Figure 5G) showed no significant difference between groups. We further analyzed their firing properties looking at the instantaneous firing of these neurons. We found that SNr-PV+ neurons in 6-OHDA conditions usually present episodes of high instantaneous firing rate alternating with periods of silence (MW-U test; p = 0.0056) (Figure 5H). Accordingly, pause analysis (see STAR Methods for details) reveals an increase in both the percentage of time in pause (MW-U; p < 0.0001) (Figure 5I) and the mean pause duration (MW-U; p = 0.0185) (Figure 5J) in 6-OHDA mice. Similarly, using the surprise method of burst detection, we revealed that the number of bursts (MW-U test; p < 0.0001) (Figure 5K) and the percentage of spike in burst were also significantly higher in 6-OHDA mice with 75% of spike in burst compared with only 30% in sham mice (MW-U test; p < 0.0001) (Figure 5L). Altogether, these results show that, after dopamine lesion, SNr-PV+ neurons discharge

Please cite this article in press as: Delgado-Zabalza et al., Targeting parvalbumin-expressing neurons in the substantia nigra pars reticulata restores motor function in parkinsonian mice, Cell Reports (2023), https://doi.org/10.1016/j.celrep.2023.113287

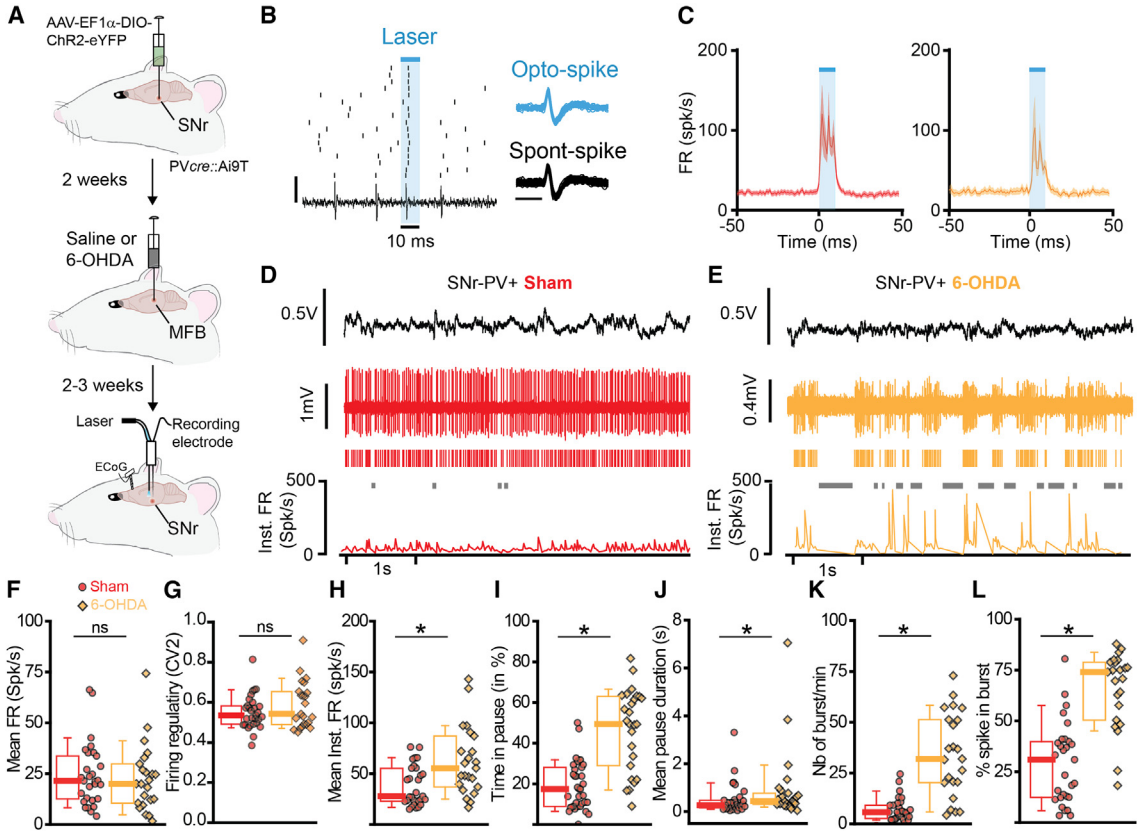

Figure 5. The *in vivo* firing pattern of identified SNr-PV+ neurons is altered in 6-OHDA mice

(A) Schematic of the experimental design used for *in vivo* recording and opto-tagging.

(B) Raster diagram of a ChR2-expressing SNr-PV+ neuron.

(C) Averaged opto-excitatory responses of SNr-PV+ cells from sham (red, n = 29) and 6-OHDA (orange, n = 23) mice.

(D and E) Typical single-unit activity of a SNr-PV+ neuron recorded in sham (D) and 6-OHDA mice (E). From top to bottom: ECoG, raw single unit trace, raster plot, and instantaneous frequency plot. All neurons were recorded under isoflurane anesthesia in similar brain state. Gray bars indicate pauses in activity.

(F and G) Population data of the mean firing rate (F) and firing regularity (CV2; G) for SNr-PV+ neurons recorded from sham (n = 29) and 6-OHDA (n = 23) mice.

(H) Population data.

(I and J) Graphs illustrating the time in pause (in %) and the mean pause duration.

(K) Number of bursts per minute in both sham and 6-OHDA mice.

(L) Graph showing the percentage of spike in burst. All neurons included were opto-tagged. Box-and-whisker plots indicate medians, interquartile range and 10%–90% ranges values. *p < 0.05. ns, not significant. See Table S2 for more details and statistical information.

in vivo in a burst-pause mode of firing. These *in vivo* data contrast with the *ex vivo* data showing a strong reduction in the intrinsic excitability of SNr-PV+ in 6-OHDA mice. To understand the function of NALCN on the activity of SNr-PV+ neurons *in vivo*, we performed an experiment in which we applied the NALCN blocker (L703,606) via a canula in control mice and we recorded opto-tagged SNr-PV+ neurons before, during, and after blockade of these channels (Figure S4). We observed that inhibition of these channels induced a significant decrease in the firing rates of these neurons (Friedman test, F = 9.33; p = 0.0055) (Figure S4C), as well as a decrease in firing regularity (Friedman test, F = 12; p = 0.0001) (Figure S4D). However, only a tendency in the reduction in number of burst/minute (Friedman test, F = 5.20; p = 0.0741) (Figure S4E) was observed in these neurons, probably because of the low number of recordings (n = 6). This result suggest that the predominant burst-pause pattern observed *in vivo* in dopamine-depleted mice is most likely because of altered glutamatergic inputs to the SNr, rather than only the lower excitability of SNr-PV+ neurons.

The pathological activity of SNr-PV+ neurons observed *in vivo* is driven by glutamatergic inputs

It is largely acknowledged that the main source of glutamatergic inputs to the SNr arise from the subthalamic nucleus (STN)[16] and that this glutamatergic pathway contributes to the pathological activity of BG output neurons in PD.[43,44] Thus, to identify whether glutamatergic inputs impinging on SNr-PV+ neurons contributed to their pathological activity in parkinsonian states *ex vivo*, we performed electrical stimulation experiments in which we placed the electrode between the STN and the SNr and we blocked inhibitory transmission by perfusion of CGP (1 μM) and GABAzine (10 μM); (Figure S5A). Thereby, we employed a cortical

Please cite this article in press as: Delgado-Zabalza et al., Targeting parvalbumin-expressing neurons in the substantia nigra pars reticulata restores motor function in parkinsonian mice, Cell Reports (2023), https://doi.org/10.1016/j.celrep.2023.113287

slow wave activity protocol inspired from *in vivo* recordings in anesthetized 6-OHDA mice[45] (Figure S5B). We first look at the impact of this burst pattern of stimulation on the firing activity of SNr-PV+ neurons in cell-attached configuration. We observed that glutamatergic inputs (putatively from the STN) induced a stronger increase in the firing rate of SNr-PV+ neurons of 6-OHDA mice compared with control ones (linear regression, $F = 5.388$; $p = 0.0304$) (Figures S5C and S5D), suggesting that these inputs have a stronger impact on the firing activity of SNr-PV+ with reduced autonomous pacemaking capabilities. We also analyzed the charge of EPSCs during trains and found a significantly bigger charge in dopamine depleted mice (MW-U test; $p = 0.0074$) (Figures S5E and S5F), suggesting that glutamatergic transmission to SNr-PV+ neurons is augmented in dopamine-depleted mice. To ultimately test whether the glutamatergic tone is responsible for the increase bursting activity of SNr-PV+ neurons observed in our *in vivo* data, we locally infused glutamatergic receptor antagonists (DNQX, 200 μM; D-AP5, 500 μM) onto identified (opto-tagged) and putative (characterized by their burst-pause activity pattern) SNr-PV+ neurons in both conditions (Figure 6A). We compared the firing rate and pattern of SNr-PV+ neurons in sham and 6-OHDA mice in baseline (Figures 6B and 6C) and when glutamatergic transmission was blocked by local infusion in the SNr of DNQX and D-AP5 (Figures 6B and 6C), which selectively block AMPA/Kainate and NMDA receptors, respectively. In sham mice, blockade of glutamatergic transmission, presumably from the STN-SNr pathway induced a significant reduction of the firing rate of SNr-PV+ neurons in sham mice (Friedman test, $F = 7.714$; $p = 0.0207$) (Figure 6D). However, the same manipulation induced a strong reduction of the firing rate of these neurons in 6-OHDA mice (Friedman test, $F = 20.46$; $p < 0.0001$) (Figure 6D). In line with this, the same reduction was observed when analyzing the mean instantaneous firing rates in SNr-PV+ cells in 6-OHDA mice (Friedman test, $F = 22.5$; $p < 0.0001$) (Figure 6E). Blocking glutamatergic transmission also increased the percentage of time spent in pause in 6-OHDA mice (Friedman test, $F = 17.23$; $p = 0.0002$) (Figure 6F), as well as the mean pause (Friedman test, $F = 17.08$; $p = 0.0002$) (Figure 6G). These results propose that, in the absence of a glutamatergic drive, SNr-PV+ cells from 6-OHDA mice spend more time silent compared with those from control mice, presumably because of their reduced intrinsic excitability. The analysis of the number of bursts and the number of spikes per burst showed no significant impact of glutamatergic transmission blockade in sham animals, while these two parameters were dramatically reduced in 6-OHDA animals (Nb of burst/min: Friedman test, $F = 17.74$; $p = 0.0001$; percent spike in burst: Friedman test, $F = 12.38$; $p = 0.002$) (Figure 6 H, I). These results are in agreement with the literature showing that STN lesion and functional inhibition were able to normalize the firing pattern of SNr neurons,[25,46] even if these studies did not differentiate distinct SNr subpopulations. Together, these data argue that in parkinsonian conditions, SNr-PV+ neurons display irregular and burst-pause firing patterns *in vivo* caused by glutamatergic inputs. Importantly, blocking glutamate receptors *in vivo* unmasked the intrinsic hypoactive state of SNr-PV+ neurons in 6-OHDA as in our *in vitro* data, supporting that change in the network activity principally drive the pathological activity of these cells in experimental parkinsonism.[47]

Chemogenetic inhibition of SNr-PV+ neurons is sufficient to ameliorate motor dysfunction in parkinsonian mice

We then wanted to test whether manipulation of SNr-PV+ neurons' activity is sufficient to restore motor function in hemiparkinsonian mice. For that, we used two behavioral tests, the cylinder test, which addresses motor asymmetry, and the open-field test for general locomotor activity. When placed in a cylinder, sham mice explore their vertical environment using both forelimbs symmetrically, while in hemi-lateral dopamine-depleted mice, forelimb use is asymmetric, e.g., the forelimb contralateral to the 6-OHDA injection is reduced relative to the ipsilateral forelimb (two-way ANOVA; interaction: $F_{(1,18)} = 18.68$; $p = 0.004$) (Figures S6A and S6B). In addition, while sham mice exhibit very little 360° rotations, 6-OHDA mice show a propensity to rotate toward the ipsilateral side of the lesion (MW-U test; $p = 0.0002$) (Figure S6C), a characteristic of dopamine imbalance between the dopamine-intact and the dopamine-depleted hemisphere. In the open field test, 6-OHDA mice display hypolocomotor behavior (Figure S6D) evidenced by a reduction in the total distance traveled (MW-U test; $p = 0.0004$) (Figure S6E), mean locomotion velocity (MW-U test; $p = 0.004$) (Figure S6F), and an increase in the number of ipsilateral rotations per minute (MW-U test; $p = 0.004$) (Figure S6G).

Non-selective chemogenetic manipulation of BG outputs has proven efficiency in the reduction of motor symptoms in rodent models of PD.[48] We further tested whether manipulating only the activity of SNr-PV+ neurons could be sufficient to restore motor functions in 6-OHDA mice. We assessed the behavioral effect of chemogenetic excitation or inhibition of these neurons via unilateral expression of excitatory or inhibitory designer receptors activated only by designer drugs (DREADDs) using Q9
Cre-dependent viral vectors to restrict the expression in SNr-PV+ cells. Three groups of mice were injected with AAV-DIO-eYFP, AAV-DIO-hM3Dq-mCitrine, or AVV-DIO-hM4Di-mCitrine viral vectors in the SNr of PVcreAi9T mice. These three groups of mice received a unilateral injection of 6-OHDA 2 weeks later. Then, the impact of chemogenetic manipulation of SNr-PV+ neurons was assessed 2–3 weeks after 6-OHDA injection by the cylinder and the open-field tests (Figure 7A). All mice were injected intraperitoneally (i.p.) with CNO (2 mg/kg) or saline in a randomized manner and were tested once in each test to avoid habituation with a delay of at least 24 h. Chemogenetic excitation (hM3D(Gq)) of SNr-PV+ cells from 6-OHDA mice did not induce any amelioration on motor asymmetry (Figures 7B and 7C). Similar results were obtained in mice expressing a control vector. The apparent dissociation between the *ex vivo* increase of firing rate in SNr-PV+ neurons induced by hM3D(Gq) activation and the absence of behavioral effect could be due to an across-subject comparison used in this study. Nevertheless, chemogenetic inhibition (hM4D(Gi)) of SNr-PV+ cells increased significantly the use of the contralateral paw to the lesion (two-way ANOVA, interaction $F_{(2, 13)} = 16.26$; $p = 0.0003$; Sidak's post hoc test, $p < 0.0001$) (Figure 7C), such that motor asymmetry was corrected with this strategy. Likewise, we observed a significant decrease on the number of ipsilateral rotations in mice expressing inhibitory DREADDs (two-way ANOVA, interaction $F_{(2, 13)} = 6.3$; $p = 0.0122$; Sidak's post hoc test, $p = 0.0014$)

Please cite this article in press as: Delgado-Zabalza et al., Targeting parvalbumin-expressing neurons in the substantia nigra pars reticulata restores motor function in parkinsonian mice, Cell Reports (2023), https://doi.org/10.1016/j.celrep.2023.113287

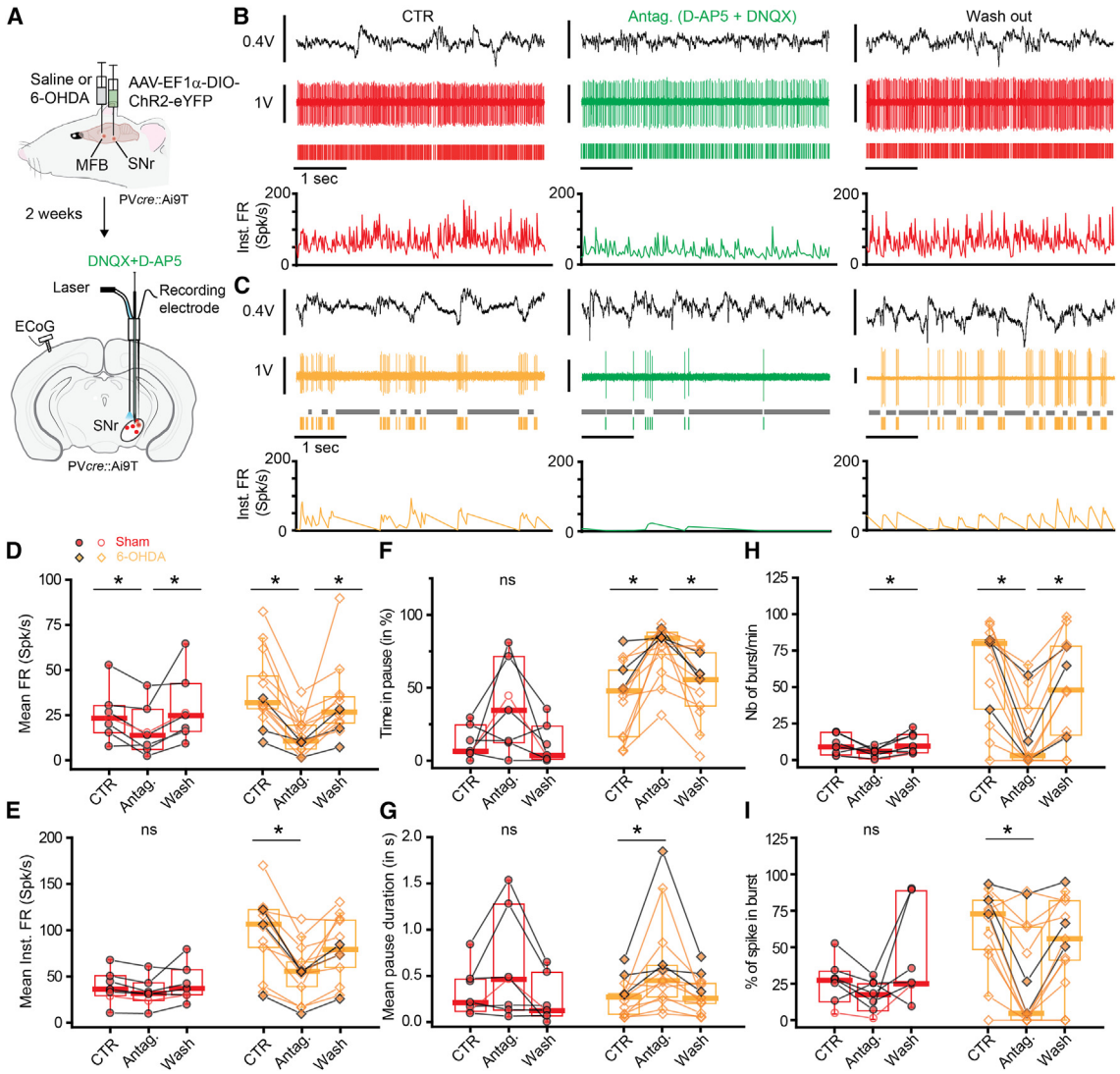

Figure 6. Pharmacological blockade of glutamatergic transmission strongly reduces SNr-PV+ neuron's rate and bursting activity *in vivo* in dopamine-depleted mice Q16

(A) Diagram of the experimental design followed for *in vivo* recordings.

(B and C) Typical single-unit activities of SNr-PV+ cells from sham (red, top) and 6-OHDA (orange, bottom) mice before (CTR), during local infusion of blockers (Antag.) and after the drugs perfusion (wash out). All neurons were recorded under similar cortical activity as observed in electrocorticograms (ECoG).

(D) Mean firing rates of SNr-PV+ neurons from sham (n = 7) and 6-OHDA (n = 13) mice before (CTR), during (Antag.), and after (Wash) DNQX+D-AP5 infusions.

(E) Population data showing greater reduction in instantaneous firing rates of SNr-PV+ cells in 6-OHDA mice when blocking glutamatergic inputs compared with sham animals.

(F) Graph illustrating the time during which neurons were in pause (silent) over the total time of recording.

(G) Plot showing the mean pause duration.

(H) Number of bursts per minute in both conditions.

(I) Graph showing the percentage of spike in burst. Filled circles (n = 6/7) and diamonds (n = 3/13) indicate the neurons that were opto-tagged, empty circles/diamonds represent putative SNr-PV+ neurons. Box-and-whisker plots indicate medians, interquartile range and 10%–90% range values. *p < 0.05, Friedman test with Dunn's post hoc test. ns, not significant. See Table S2 for more details and statistical information. See also Figure S5.

(Figure 7D). As expected, mice expressing Gi DREADDs also showed an improvement in locomotion behavior in the open field test compared with control-injected (eYFP) and chemogenetic excitation groups (Figures 7E–7H). These results support the conclusion that reducing abnormal bursting activity of SNr-PV+ neurons is sufficient to ameliorate parkinsonian dysfunctions in 6-OHDA mice and suggest that such abnormal bursting activity is pathological for motor functions.[49,50]

Immunohistochemical experiments were performed to confirm the selective expression of the chemogenetic vectors in SNr-PV+ neurons (Figures S7A and S7B). In addition, perfusion of CNO (10 μM) in acute brain slices significantly increases

Please cite this article in press as: Delgado-Zabalza et al., Targeting parvalbumin-expressing neurons in the substantia nigra pars reticulata restores motor function in parkinsonian mice, Cell Reports (2023), https://doi.org/10.1016/j.celrep.2023.113287

CellPress
OPEN ACCESS

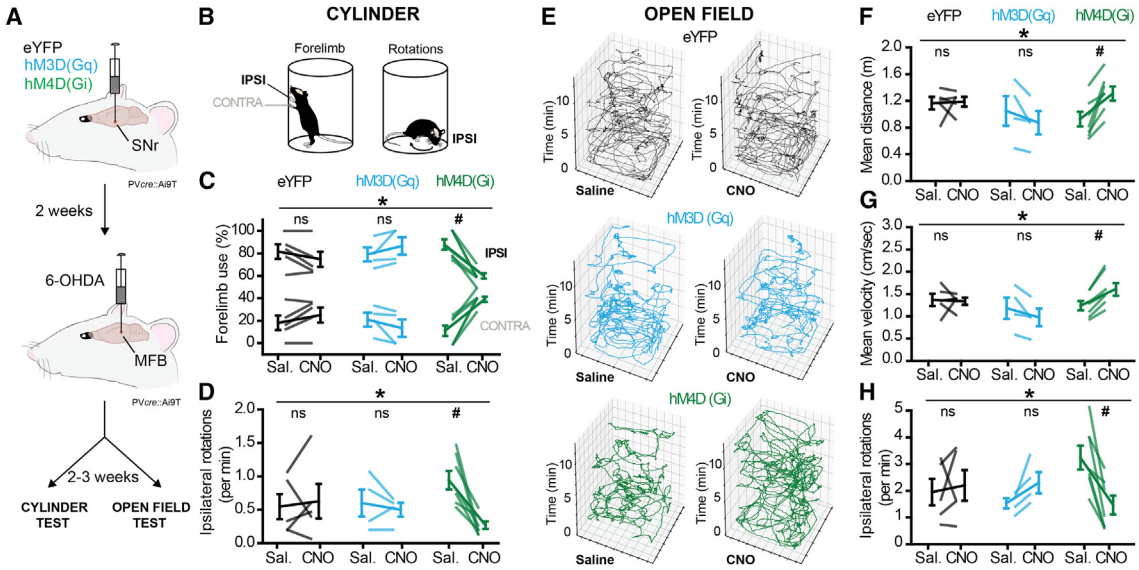

Figure 7. Chemogenetic inhibition of SNr-PV+ neurons rescues motor deficits of parkinsonian mice

(A) Schematic of the chemogenetic and behavioral experiments. Three groups of unilateral 6-OHDA-injected mice received either a Cre-dependent control virus (5 mice), excitatory DREADDs (4 mice), or inhibitory DREADDs (7 mice) in the SNr and were tested in the cylinder and open field test.

(B–D) Two parameters were analyzed in the cylinder test. The percentage of IPSI/CONTRA-lateral forelimb use (C) and the ipsilateral rotations (D) after saline (Sal.) or chemogenetic manipulation with CNO (2 mg/kg).

(E) Position of 6-OHDA mice expressing control (eYFP, top), excitatory (hM3D(Gq), middle) or inhibitory (hM4D(Gi), bottom) DREADDs in an open field over 15 min after injection of saline (left) or CNO (right).

(F–H) Average distance traveled (F), mean velocity (G), and number of ipsilateral rotations (H) in 6-OHDA mice treated with saline and CNO. Group data represents mean ± SEM. *p < 0.05, two-way ANOVA; #p < 0.05, Sidak's post hoc test. ns, not significant. See Table S2 for more details and statistical information. See also Figures S6 and S7.

or reduces the firing rate of SNr-PV+ neurons expressing Gq DREADDs (WSR test; p = 0.0156) (Figures S7C and S7D) or Gi DREADDs (WSR test; p = 0.0020) (Figures S7E and S7F), respectively, and thus validate our experimental strategy. In addition, we performed *in vivo* recordings from 6-OHDA mice expressing in SNr-PV+ neurons both DIO-ChR2 and inhibitory DREADDs. Mice were injected i.p. with 2 mg/kg of CNO (Figures S7G and S7K) and, 30 min after injection, we analyzed different electrophysiological parameters such as the FR and CV2. In five of six recorded neurons, the firing rate decreased under CNO (WSR test; p = 0.0938) (Figure S7I), while no significant modification of the firing regularity was observed (WSR test; p = 0.1563) (Figure S7J). However, the number of bursts/minute was significantly reduced after CNO injections (WSR test; p = 0.0313) (Figure S7K). This validation confirms our strategy and reinforces our behavioral results.

DISCUSSION

Molecular and functional diversity in the substantia nigra

The cellular complexity of the SNr has been a long-standing question. Several studies have established that the SNr is composed of several classes of neurons based on molecular markers expression,[5,6] their projection targets,[7,8] or their selective involvement in motor and cognitive brain functions.[7,16,51,52] Among, these neuronal populations, SNr-PV+ neurons represent the largest population, with almost two-thirds of the total number of SNr neurons.[5,8,16] This population is also predominantly found in the dorso-lateral portion of the SNr,[4,16] which corresponds with the sensorimotor domain of the nucleus[4,34,35] and innervates predominantly motor-related nuclei in the diencephalon and the brainstem.[16] Our anatomical characterization of the distribution and projectome of SNr-PV+ neurons agree with these previous findings. Distinct electrophysiological profiles of SNr neurons based on their molecular identity[53] or their projection targets[7,8] have been described. However, so far it has not been demonstrated that a population of neurons in the SNr, notably PV+ neurons, have a distinctive electrophysiological signature, as they display a faster autonomous firing *ex vivo* compared with non-PV expressing SNr cells (Figure 2). This feature is further explained by the amount of inward current supported by NALCN channels in these neurons. Regarding the function of SNr-PV+ neurons, a recent study demonstrated that this cell type is mainly involved in motor control when the animal is awake,[16] suggesting that this population could be more susceptible in PD. In line with this theory, we found a selective decrease in the intrinsic excitability of SNr-PV+ neurons in 6-OHDA mice.

Experimental parkinsonism dampens autonomous pacemaking in SNr-PV+ neurons

The decrease in the firing rate of SNr-PV+ neurons from dopamine-depleted mice observed here is consistent with previous

Please cite this article in press as: Delgado-Zabalza et al., Targeting parvalbumin-expressing neurons in the substantia nigra pars reticulata restores motor function in parkinsonian mice, Cell Reports (2023), https://doi.org/10.1016/j.celrep.2023.113287

works in the SNr.[10,21] Similar decreases in cell excitability in experimental parkinsonism have been reported in other extra-
Q10 striatal BG nuclei, such as the globus pallidus externa (GPe)[54,55] and the STN.[56] In the GPe, the nature of the ionic(s) conductance(s) impacted by the loss of dopamine has not been investigated, but in the STN it has been shown that dopamine depletion triggers NMDA-dependent activation of K_{ATP} channels, leading to STN neurons' hypoactivity.[56] Here, we provide evidence that NALCN channels are dysfunctional in SNr-PV+ neurons after dopamine depletion. We also showed that the amount of NALCN currents is much smaller in SNr-PV- neurons, which can explain why this cell type activity is not impacted in 6-OHDA mice. NALCN conductances have been shown to regulate the level of depolarization of the membrane potential and control the bursting activity of many neuronal cell types throughout the brain.[12,57–59] In the BG, NALCN channels are en-
Q11 riched in pacemaking nuclei (GPe, internal globus pallidus, STN,
Q12 substantia nigra pars compacta [SNc], and SNr), but their functional role has been mainly studied in the SN.[12,59–61] Pharmacological blockade of these channels in SNc and SNr neurons induces a strong hyperpolarization of the membrane potential and thus completely inhibits autonomous pacemaking.[9,59,60] In SNc neurons, their location on proximal dendrites plays in the control of glutamate-induced bursting activity.[61] These channels are the target of several modulatory pathways and G-protein-coupled receptors,[12,60] and, in the SNc, they are inhibited by Gi/o-protein-coupled D2 dopamine and GABAB receptors.[60] Furthermore, knock-out animal models for NALCN channels show motor impairments reminiscent of PD motor symptoms,[62,63] supporting a key role of these channels in motor functions.

Several non-exclusive mechanisms can contribute to NALCN channel dysfunction in SNr-PV+ neurons, such as a direct loss of dopaminergic modulation of SNr neuron excitability, a network-driven loss of neuronal excitability, or a maladaptive reduction of NALCN channel expression in response to SNr-inputs pathological activity. Several hypotheses can be considered. The most straightforward is a direct loss of dopamine modulation of SNr neurons from the so-called ultrashort dopaminergic pathway, as dendritic release of DA has been shown to increase the firing activity of SNr through the activation of post-synaptic D1 dopamine receptors.[10] In line with this hypothesis, a reduction in firing rate of SNr neurons under the blockade of D1 and D2 receptors and in experimental parkinsonism in juvenile mice has been reported recently.[64] However, a direct dopamine modulation of NALCN channels remains to be demonstrated. Another possibility is the decrease of substance P release due to the hypoactivity of the direct-pathway. Indeed, substance P is known to excite SNr neurons by activating neurokinin-1 receptors (NK1R).[65] Furthermore, NALCN channels are positively modulated by NK1R.[66] Thus, reduction of the activity of the direct pathway could lead to reduced modulation of these channels by SP resulting in firing rate decrease. Finally, the reduction of SNr-PV+ neuron excitability can be a maladaptive response to the augmented glutamatergic drive of STN neurons and the increase activity of the STN-SNr synaptic pathway in parkinsonian conditions.[44,67] Considering that blocking glutamatergic transmission in the SNr almost totally abolishes the bursting activity pattern of SNr-PV+ neurons in parkinsonian mice, this hypothesis might be the most accurate.

Reduced autonomous pacemaking favors network-driven pathological activity in SNr-PV+ neurons *in vivo*

Loss of intrinsic excitability after dopamine depletion has been reported in several BG nuclei,[54,56] including in the SNr.[21] In the STN, the consequence of this decrease in autonomous pacemaking is that STN neurons become entrained by pathological synaptic inputs.[56,68] Our data support the same conclusion regarding SNr-PV+ neurons, which display reduced excitability *ex vivo* but arbor burst-pause activity *in vivo* in dopamine-depleted mice. This change in pattern of activity is the electrophysiological hallmark of PD and has been observed in several animal models,[24,27] as well as in idiopathic PD.[43] Interestingly, reduction of firing frequency in SNr neurons has been reported to occur in prodromal stages of the disease, suggesting that alteration in firing rate occurs first during the progression of PD,[24] while changes in pattern of activity occur later and might be the consequences of maladaptive compensatory plasticity in the BG circuit. In addition to these temporal aspects of the pathophysiology of PD, our data also highlight the need to take the cellular complexity of the SNr into account, as distinct neuronal subpopulations may not be affected in the same way in experimental parkinsonism.

Counteracting pathological activity in the output of the BG in a cell-type manner is sufficient to rescue motor function

Oscillatory and synchronous activity patterns in the BG have been associated with the severity of PD motor symptoms.[49,69,70] In addition, a recent study investigated the correlation between the pattern of activity of STN neurons and the severity of motor symptoms in PD patients[71] and found that burst-pause STN neurons were positively correlated with PD motor symptoms. In the present study, we show that SNr-PV+ neurons display a burst-pause mode of firing activity in dopamine-depleted mice that constitute one more piece of evidence of the pathological nature of the burst-pause pattern of activity, which can be seen as an independent electrophysiological markers of PD pathophysiology. Global pharmacological inactivation of the SNr using muscimol infusion in MPTP-monkey has been proven efficient to reduce motor symptoms.[50] Other experimental interventions have been tested more recently. Chemogenetic inhibition of both the EPN and SNr has also been a successful strategy to reduce motor symptoms in hemi-parkinsonian rodents,[48] and local SNr pharmacological blockade of NMDA receptors produced similar outcome.[67] All these results point out that reducing SNr neuron's activity is the most efficient strategy to alleviate PD motor symptoms. Our results also support this conclusion; when we blocked AMPA and NMDA receptors in the SNr while monitoring the activity of SNr-PV+ we observed a strong decrease in burst-pause activity, suggesting that counteracting the pathological activity of these neurons could be responsible for the decrease in PD symptoms. However, in the studies mentioned above, the neuronal diversity of the SNr has not been taken into consideration. Given the division of labor between SNr-PV+ and SNr–GAD2+ neurons in the regulation of motor control between sleep-wake cycle,[16]

cell-type-selective manipulations to restore PD motor function without generating unwanted side effects is needed. We showed that inhibiting the PV+ neuronal subpopulation of the SNr induced a considerable restoration of motor function in hemi-parkinsonian mice, with a strong decrease in ipsilateral rotations, locomotor activity, and symmetrical use of forelimb paws during exploration. In the same line, both our pharmacological and chemogenetic data support the hypothesis that it is better to have no BG output rather than a pathological one.[72]

Clinical relevance

In line with the established functions of SNr-PV+ neurons in motor control and epileptic seizures,[16,51] deep brain stimulation (DBS) of the SNr has been shown to decrease motor symptoms[73,74] and exert long-lasting suppression of seizures[75] in rodents, such as the SNr is nowadays considered as a promising target of choice for DBS electrode implantation.[76] Some studies have also pointed out that stimulation location is a critical factor for the effectiveness of SNr DBS.[77–79] Our data suggest that targeting the dorsolateral portion of the SNr should be the most efficient to restore proper motor control using SNr-DBS. It will be also interesting to use optical DBS of ChR2-expressing SNr-PV+ to prove the therapeutic potential of this neuronal population for the treatment of movement disorders.

Limitations of the study

Although we demonstrated that SNr-PV+ have a decreased intrinsic excitability in PD mice, we did not identify the main cause of this reduction. Because SNr-PV+ express D1 dopamine receptors, which increase their firing rate,[10] a direct loss of dopaminergic modulation could be the main trigger of the altered excitability of SNr-PV+ neurons, but our study cannot exclude either a maladaptive response to exacerbated glutamatergic inputs as a contributing factor. However, it is technically challenging to selectively manipulate presynaptic pathways, such as STN inputs, without having complex networks effects. Another limitation of our study is the lack of *in vivo* characterization of the other SNr cell population (SNr-PV–) to determine if the pattern of these neurons is also impacted in experimental parkinsonism. Studying the activity of this cell-type *in vivo* could be of interest in the future regarding its involvement in motor and non-motor dysfunctions in PD.

STAR★METHODS

Detailed methods are provided in the online version of this paper and include the following:

SUPPLEMENTAL INFORMATION

Supplemental information can be found online at https://doi.org/10.1016/j.celrep.2023.113287.

ACKNOWLEDGMENTS

This work was supported by the France Parkinson (to J.B. and L.D.; grant #2019-0558), Euskampus, University of the Basque Country (L.D. predoctoral grant) and Fondation de France (to J.B.; grant #00096655), the French government in the framework of the University of Bordeaux's IdEx "Investments for the Future - France 2030" program/GPR BRAIN_2030 (to J.B.). This research was also conducted in the scope of the Transborder Joint Laboratory (LTC) "non-motor CoMorbidities in Parkinson's Disease (CoMorPD) (to J.B. and C.M.). We also acknowledge the institutional support provided by the University of Bordeaux and the Centre National de Recherche Scientifique (CNRS). Q13
We are also grateful to the Broca center animal facility for taking care of the animals included in this study.

AUTHOR CONTRIBUTIONS

J.B., C.M., and L.D. conceived the study and designed the experiments; L.D., N.M., and M.G. conducted anatomical and electrophysiological experiments; L.D., G.D., and C.G. conducted behavioral experiments; L.D., N. M., M.G., and C.G. analyzed the data; L.D., J.B., N.M., and C.M. wrote the manuscript.

DECLARATION OF INTERESTS

The authors declare no conflicts of interest.

INCLUSION AND DIVERSITY Q8

We support inclusive, diverse, and equitable conduct of research.

Received: March 24, 2023
Revised: August 31, 2023
Accepted: September 29, 2023

REFERENCES

1. Freeze, B.S., Kravitz, A.V., Hammack, N., Berke, J.D., and Kreitzer, A.C. (2013). Control of basal ganglia output by direct and indirect pathway projection neurons. J. Neurosci. *33*, 18531–18539. https://doi.org/10.1523/JNEUROSCI.1278-13.2013.
2. Gerfen, C.R. (1992). The neostriatal mosaic: Multiple levels of compartmental organization. J. Neural. Transm. Suppl. *36* (*36*), 43–59. https://doi.org/10.1007/978-3-7091-9211-5_4.
3. Reiner, A., and Anderson, K.D. (1993). Co-occurrence of γ-aminobutyric acid, parvalbumin and the neurotensin-related neuropeptide LANT6 in

pallidal, nigral and striatal neurons in pigeons and monkeys. Brain Res. *624*, 317–325. https://doi.org/10.1016/0006-8993(93)90096-6.

4. Rajakumar, N., Elisevich, K., and Flumerfelt, B.A. (1994). Parvalbumin-containing GABAergic neurons in the basal ganglia output system of the rat. J. Comp. Neurol. *350*, 324–336. https://doi.org/10.1002/cne.903500214.
5. González-Hernández, T., and Rodríguez, M. (2000). Compartmental organization and chemical profile of dopaminergic and GABAergic neurons in the substantia nigra of the rat. J. Comp. Neurol. *421*, 107–135. https://doi.org/10.1002/(SICI)1096-9861(20000522)421:1<107::AID-CNE7>3.0.CO;2-F.
6. Saunders, A., Macosko, E.Z., Wysoker, A., Goldman, M., Krienen, F.M., de Rivera, H., Bien, E., Baum, M., Bortolin, L., Wang, S., et al. (2018). Molecular Diversity and Specializations among the Cells of the Adult Mouse Brain. Cell *174*, 1015–1030.e16. https://doi.org/10.1016/j.cell.2018.07.028.
7. Rizzi, G., and Tan, K.R. (2019). Synergistic Nigral Output Pathways Shape Movement. Cell Rep. *27*, 2184–2198.e4. https://doi.org/10.1016/j.celrep.2019.04.068.
8. McElvain, L.E., Chen, Y., Moore, J.D., Brigidi, G.S., Bloodgood, B.L., Lim, B.K., Costa, R.M., and Kleinfeld, D. (2021). Specific populations of basal ganglia output neurons target distinct brain stem areas while collateralizing throughout the diencephalon. Neuron *109*, 1721–1738.e4. https://doi.org/10.1016/j.neuron.2021.03.017.
9. Atherton, J.F., and Bevan, M.D. (2005). Ionic mechanisms underlying autonomous action potential generation in the somata and dendrites of GABAergic substantia nigra pars reticulata neurons in vitro. J. Neurosci. *25*, 8272–8281.
10. Zhou, F.W., Jin, Y., Matta, S.G., Xu, M., and Zhou, F.M. (2009). An ultra-short dopamine pathway regulates basal ganglia output. J. Neurosci. *29*, 10424–10435. https://doi.org/10.1523/JNEUROSCI.4402-08.2009.
11. Lutas, A., Birnbaumer, L., and Yellen, G. (2014). Metabolism regulates the spontaneous firing of substantia nigra pars reticulata neurons via KATPand nonselective cation channels. J. Neurosci. *34*, 16336–16347. https://doi.org/10.1523/JNEUROSCI.1357-14.2014.
12. Lutas, A., Lahmann, C., Soumillon, M., and Yellen, G. (2016). The leak channel NALCN controls tonic firing and glycolytic sensitivity of substantia nigra pars reticulata neurons. Elife *5*, e15271. https://doi.org/10.7554/eLife.15271.
13. DeLong, M.R., Crutcher, M.D., and Georgopoulos, A.P. (1983). Relations between movement and single cell discharge in the substantia nigra of the behaving monkey. J. Neurosci. *3*, 1599–1606. https://doi.org/10.1523/jneurosci.03-08-01599.1983.
14. Gulley, J.M., Kosobud, A.E.K., and Rebec, G.V. (2002). Behavior-related modulation of substantia nigra pars reticulata neurons in rats performing a conditioned reinforcement task. Neuroscience *111*, 337–349. https://doi.org/10.1016/S0306-4522(02)00018-0.
15. Jin, X., and Costa, R.M. (2010). Start/Stop Signals Emerge in Nigrostriatal Circuits during Sequence Learning Xin. Nature *23*, 1–7. https://doi.org/10.1038/nature09263.Start/Stop.
16. Liu, D., Li, W., Ma, C., Zheng, W., Yao, Y., Tso, C.F., Zhong, P., Chen, X., Song, J.H., Choi, W., et al. (2020). A common hub for sleep and motor control in the substantia nigra. Science *367*, 440–445. https://doi.org/10.1126/science.aaz0956.
17. Albin, R.L., Young, A.B., Penney, J.B., Roger, L.A., and Young, B.B. (1989). The functional anatomy of basal ganglia disorders. Trends Neurosci. *12*, 366–375.
18. DeLong, M.R. (1990). Primate models of movement disorders of basal ganglia origin. Trends Neurosci. *13*, 281–285. https://doi.org/10.1016/0166-2236(90)90110-V.
19. Wang, Y., Zhang, Q.J., Liu, J., Ali, U., Gui, Z.H., Hui, Y.P., Chen, L., and Wang, T. (2010). Changes in firing rate and pattern of GABAergic neurons in subregions of the substantia nigra pars reticulata in rat models of Parkinson's disease. Brain Res. *1324*, 54–63. https://doi.org/10.1016/j.brainres.2010.02.008.
20. Rohlfs, A., Nikkhah, G., Rosenthal, C., Rundfeldt, C., Brandis, A., Samii, M., and Löscher, W. (1997). Hemispheric asymmetries in spontaneous firing characteristics of substantia nigra pars reticulata neurons following a unilateral 6- hydroxydopamine lesion of the rat nigrostriatal pathway. Brain Res. *761*, 352–356. https://doi.org/10.1016/S0006-8993(97)00475-7.
21. Faynveitz, A., Lavian, H., Jacob, A., and Korngreen, A. (2019). Proliferation of Inhibitory Input to the Substantia Nigra in Experimental Parkinsonism. Front. Cell. Neurosci. *13*, 417. https://doi.org/10.3389/fncel.2019.00417.
22. Wichmann, T., Bergman, H., Starr, P.A., Subramanian, T., Watts, R.L., and DeLong, M.R. (1999). Comparison of MPTP-induced changes in spontaneous neuronal discharge in the internal pallidal segment and in the substantia nigra pars reticulata in primates. Exp. Brain Res. *125*, 397–409.
23. Aristieta, A., Ruiz-Ortega, J.A., Miguelez, C., Morera-Herreras, T., and Ugedo, L. (2016). Chronic L-DOPA administration increases the firing rate but does not reverse enhanced slow frequency oscillatory activity and synchronization in substantia nigra pars reticulata neurons from 6-hydroxydopamine-lesioned rats. Neurobiol. Dis. *89*, 88–100. https://doi.org/10.1016/j.nbd.2016.02.003.
24. Willard, A.M., Isett, B.R., Whalen, T.C., Mastro, K.J., Ki, C.S., Mao, X., and Gittis, A.H. (2019). State transitions in the substantia nigra reticulata predict the onset of motor deficits in models of progressive dopamine depletion in mice. Elife *8*, e42746. https://doi.org/10.7554/eLife.42746.
25. Murer, M.G., Riquelme, L.A., Tseng, K.Y., and Pazo, J.H. (1997). Substantia nigra pars reticulata single unit activity in normal and 60HDA-lesioned rats: Effects of intrastriatal apomorphine and subthalamic lesions. Synapse *27*, 278–293. https://doi.org/10.1002/(SICI)1098-2396(199712)27:4<278::AID-SYN2>3.0.CO;2-9.
26. Seeger-Armbruster, S., and Von Ameln-Mayerhofer, A. (2013). Short- and long-term unilateral 6-hydroxydopamine lesions in rats show different changes in characteristics of spontaneous firing of substantia nigra pars reticulata neurons. Exp. Brain Res. *224*, 15–24. https://doi.org/10.1007/s00221-012-3285-3.
27. Lobb, C.J., and Jaeger, D. (2015). Bursting activity of substantia nigra pars reticulata neurons in mouse parkinsonism in awake and anesthetized states. Neurobiol. Dis. *75*, 177–185. https://doi.org/10.1016/j.nbd.2014.12.026.
28. Nagai, T., McGeer, P.L., and McGeer, E.G. (1983). Distribution of GABA-T-Intensive neurons in the hat forebrain and midbrain. J. Comp. Neurol. *218*, 220–238. https://doi.org/10.1002/cne.902180209.
29. Ottersen, O.P., and Storm-Mathisen, J. (1984). Glutamate- and GABA-containing neurons in the mouse and rat brain, as demonstrated with a new immunocytochemical technique. J. Comp. Neurol. *229*, 374–392. https://doi.org/10.1002/cne.902290308.
30. Smith, Y., Séguéla, P., and Parent, A. (1987). Distribution of gaba-immunoreactive neurons in the thalamus of the squirrel monkey (Saimiri sciureus). Neuroscience *22*, 579–591. https://doi.org/10.1016/0306-4522(87)90355-1.
31. Ficalora, A.S., and Mize, R.R. (1989). The neurons of the substantia nigra and zona incerta which project to the cat superior colliculus are GABA immunoreactive: A double-label study using GABA immunocytochemistry and lectin retrograde transport. Neuroscience *29*, 567–581. https://doi.org/10.1016/0306-4522(89)90131-0.
32. von Krosigk, M., Smith, Y., Bolam, J.P., and Smith, A.D. (1992). Synaptic organization of gabaergic inputs from the striatum and the globus pallidus onto neurons in the substantia nigra and retrorubral field which project to the medullary reticular formation. Neuroscience *50*, 531–549. https://doi.org/10.1016/0306-4522(92)90445-8.
33. Lynd-Balta, E., and Haber, S.N. (1994). Primate striatonigral projections: A comparison of the sensorimotor-related striatum and the ventral striatum. J. Comp. Neurol. *345*, 562–578. https://doi.org/10.1002/cne.903450407.

34. Deniau, J.M., Menetrey, A., and Charpier, S. (1996). The lamellar organization of the rat substantia nigra pars reticulata: Segregated patterns of striatal afferents and relationship to the topography of corticostriatal projections. Neuroscience *73*, 761–781. https://doi.org/10.1016/0306-4522(96)00088-7.

35. Foster, N.N., Barry, J., Korobkova, L., Garcia, L., Gao, L., Becerra, M., Sherafat, Y., Peng, B., Li, X., Choi, J.H., et al. (2021). The mouse cortico–basal ganglia–thalamic network. Nature *598*, 188–194. https://doi.org/10.1038/s41586-021-03993-3.

36. Saunders, A., Huang, K.W., and Sabatini, B.L. (2016). Globus Pallidus Externus Neurons Expressing parvalbumin Interconnect the Subthalamic Nucleus and Striatal Interneurons. PLoS One *11*, e0149798. https://doi.org/10.1371/journal.pone.0149798.

37. Tepper, J.M., and Lee, C.R. (2007). GABAergic control of substantia nigra dopaminergic neurons. Prog. Brain Res. *160*, 189–208. https://doi.org/10.1016/S0079-6123(06)60011-3.

38. Lee, J.I., Shin, H.J., Nam, D.H., Kim, J.S., Hong, S.C., Shin, H.J., Park, K., Eoh, W., Kim, J.H., and Lee, W.Y. (2001). Increased burst firing in substantia nigra pars reticulata neurons and enhanced response to selective D2 agonist in hemiparkinsonian rats after repeated administration of apomorphine. J. Kor. Med. Sci. *16*, 636–642. https://doi.org/10.3346/jkms.2001.16.5.636.

39. Hutchinson, W.D., Levy, R., Dostrovsky, J.O., Lozano, A.M., and Lang, A.E. (1997). Effects of apomorphine on globus pallidus neurons in parkinsonian patients. Ann. Neurol. *42*, 767–775. https://doi.org/10.1002/ana.410420513.

40. Hahn, S., Kim, S.W., Um, K.B., Kim, H.J., and Park, M.K. (2020). N-Benzhydryl Quinuclidine Compounds Are a Potent and Src Kinase-Independent Inhibitor of NALCN Channels. Br. J. Pharmacol. *177*. https://doi.org/10.1111/bph.15104.

41. Obeso, J.A., Rodríguez-Oroz, M.C., Rodríguez, M., Arbizu, J., and Giménez-Amaya, J.M. (2002). The basal ganglia and disorders of movement: Pathophysiological mechanisms. News Physiol. Sci. *17*, 51–55. https://doi.org/10.1152/nips.01363.2001.

42. DeLong, M.R., and Wichmann, T. (2015). Basal ganglia circuits as targets for neuromodulation in Parkinson disease. JAMA Neurol. *72*, 1354–1360. https://doi.org/10.1001/jamaneurol.2015.2397.

43. Levy, R., Hutchison, W.D., Lozano, A.M., and Dostrovsky, J.O. (2000). High-frequency synchronization of neuronal activity in the subthalamic nucleus of Parkinsonian patients with limb tremor. J. Neurosci. *20*, 7766–7775. https://doi.org/10.1523/jneurosci.20-20-07766.2000.

44. Dupuis, J.P., Feyder, M., Miguelez, C., Garcia, L., Morin, S., Choquet, D., Hosy, E., Bezard, E., Fisone, G., Bioulac, B.H., and Baufreton, J. (2013). Dopamine-dependent long-term depression at subthalamo-nigral synapses is lost in experimental parkinsonism. J. Neurosci. *33*, 14331–14341. https://doi.org/10.1523/JNEUROSCI.1681-13.2013.

45. Kovaleski, R.F., Callahan, J.W., Chazalon, M., Wokosin, D.L., Baufreton, J., and Bevan, M.D. (2020). Dysregulation of external globus pallidus-subthalamic nucleus network dynamics in parkinsonian mice during cortical slow-wave activity and activation. Wave Activity and Activation *598*, 1897–1927. https://doi.org/10.1113/JP279232.Dysregulation.

46. Tseng, K.Y., Kasanetz, F., Kargieman, L., Pazo, J.H., Murer, M.G., and Riquelme, L.A. (2001). Subthalamic nucleus lesions reduce low frequency oscillatory firing of substantia nigra pars reticulata neurons in a rat model of Parkinson's disease. Brain Res. *904*, 93–103. https://doi.org/10.1016/S0006-8993(01)02489-1.

47. Mallet, N., Delgado, L., Chazalon, M., Miguelez, C., and Baufreton, J. (2019). Cellular and Synaptic Dysfunctions in Parkinson's Disease: Stepping out of the Striatum. Cells *8*, 1005. https://doi.org/10.3390/cells8091005.

48. Assaf, F., and Schiller, Y. (2019). A chemogenetic approach for treating experimental Parkinson's disease. Mov. Disord. *34*, 469–479. https://doi.org/10.1002/mds.27554.

49. Sharott, A., Gulberti, A., Zittel, S., Tudor Jones, A.A., Fickel, U., Münchau, A., Köppen, J.A., Gerloff, C., Westphal, M., Buhmann, C., et al. (2014). Activity parameters of subthalamic nucleus neurons selectively predict motor symptom severity in Parkinson's disease. J. Neurosci. *34*, 6273–6285. https://doi.org/10.1523/JNEUROSCI.1803-13.2014.

50. Wichmann, T., and Soares, J. (2006). Neuronal firing before and after burst discharges in the monkey basal ganglia is predictably patterned in the normal state and altered in parkinsonism. J. Neurophysiol. *95*, 2120–2133. https://doi.org/10.1152/jn.01013.2005.

51. Chen, B., Xu, C., Wang, Y., Lin, W., Wang, Y., Chen, L., Cheng, H., Xu, L., Hu, T., Zhao, J., et al. (2020). A disinhibitory nigra-parafascicular pathway amplifies seizure in temporal lobe epilepsy. Nat. Commun. *11*, 923. https://doi.org/10.1038/s41467-020-14648-8.

52. Jia, T., Wang, Y.D., Chen, J., Zhang, X., Cao, J.L., Xiao, C., and Zhou, C. (2022). A nigro–subthalamo–parabrachial pathway modulates pain-like behaviors. Nat. Commun. *13*, 7756. https://doi.org/10.1038/s41467-022-35474-0.

53. Lee, C.R., and Tepper, J.M. (2007). Morphological and Physiological Properties of Parvalbumin- and Calretinin-Containing -Aminobutyric Acidergic Neurons in the Substantia Nigra. J. Comp. Neurol. *500*, 958–972.

54. Chan, C.S., Glajch, K.E., Gertler, T.S., Guzman, J.N., Mercer, J.N., Lewis, A.S., Goldberg, A.B., Tkatch, T., Shigemoto, R., Fleming, S.M., et al. (2011). HCN channelopathy in external globus pallidus neurons in models of Parkinson's disease. Nat. Neurosci. *14*, 85–92. https://doi.org/10.1038/nn.2692.

55. Hernández, V.M., Hegeman, D.J., Cui, Q., Kelver, D.A., Fiske, M.P., Glajch, K.E., Pitt, J.E., Huang, T.Y., Justice, N.J., and Chan, C.S. (2015). Parvalbumin + neurons and Npas1 + neurons are distinct neuron classes in the mouse external globus pallidus. J. Neurosci. *35*, 11830–11847. https://doi.org/10.1523/JNEUROSCI.4672-14.2015.

56. McIver, E.L., Atherton, J.F., Chu, H.Y., Cosgrove, K.E., Kondapalli, J., Wokosin, D., Surmeier, D.J., and Bevan, M.D. (2019). Maladaptive Downregulation of Autonomous Subthalamic Nucleus Activity following the Loss of Midbrain Dopamine Neurons. Cell Rep. *28*, 992–1002.e4. https://doi.org/10.1016/j.physbeh.2017.03.040.

57. Cochet-Bissuel, M., Lory, P., and Monteil, A. (2014). The sodium leak channel, NALCN, in health and disease. Front. Cell. Neurosci. *8*, 132. https://doi.org/10.3389/fncel.2014.00132.

58. Shi, Y., Abe, C., Holloway, B.B., Shu, S., Kumar, N.N., Weaver, J.L., Sen, J., Perez-Reyes, E., Stornetta, R.L., Guyenet, P.G., and Bayliss, D.A. (2016). Nalcn is a "leak" sodium channel that regulates excitability of brainstem chemosensory neurons and breathing. J. Neurosci. *36*, 8174–8187. https://doi.org/10.1523/JNEUROSCI.1096-16.2016.

59. Um, K.B., Hahn, S., Kim, S.W., Lee, Y.J., Birnbaumer, L., Kim, H.J., and Park, M.K. (2021). TRPC3 and NALCN channels drive pacemaking in substantia nigra dopaminergic neurons. Elife *10*, e70920–e70922. https://doi.org/10.7554/elife.70920.

60. Philippart, F., and Khaliq, Z.M. (2018). i/o protein-coupled receptors in dopamine neurons inhibit the sodium leak channel NALCN. Elife *7*, e40984. https://doi.org/10.7554/eLife.40984.

61. Hahn, S., Um, K.B., Kim, H.J., and Park, M.K. (2022). Proximal Dendritic Localization of NALCN Channels Underlies Tonic and Burst Firing in Nigral Dopaminergic Neurons. J. Physiol. *601*, 171–193. https://doi.org/10.1113/JP283716.

62. Kasap, M., Bonnett, K., Aamodt, E.J., and Dwyer, D.S. (2017). Akinesia and freezing caused by Na+ leak-current channel (NALCN) deficiency corrected by pharmacological inhibition of K+ channels and gap junctions. J. Comp. Neurol. *525*, 1109–1121. https://doi.org/10.1002/cne.24119.

63. Kasap, M., and Dwyer, D.S. (2021). Na+ leak-current channel (NALCN) at the junction of motor and neuropsychiatric symptoms in Parkinson's disease. J. Neural. Transm. *128*, 749–762. https://doi.org/10.1007/s00702-021-02348-6.

64. Cáceres-Chávez, V.A., Hernández-Martínez, R., Pérez-Ortega, J., Herrera-Valdez, M.A., Aceves, J.J., Galarraga, E., and Bargas, J. (2018). Acute dopamine receptor blockade in substantia nigra pars reticulata: A possible model for drug-induced parkinsonism. J. Neurophysiol. *120*, 2922–2938. https://doi.org/10.1152/jn.00579.2018.

65. Nalivaiko, E., Michaud, J.C., Soubrié, P., Le Fur, G., and Feltz, P. (1997). Tachykinin neurokinin-1 and neurokinin-3 receptor-mediated responses in guinea-pig substantia nigra: An in vitro electrophysiological study. Neuroscience *78*, 745–757. https://doi.org/10.1016/S0306-4522(96)00625-2.

66. Lu, B., Su, Y., Das, S., Wang, H., Wang, Y., Liu, J., and Ren, D. (2009). Peptide neurotransmitters activate a cation channel complex of NALCN and UNC-80. Nature *23*, 1–7. https://doi.org/10.1038/nature07579.

67. Sitzia, G., Mantas, I., Zhang, X., Svenningsson, P., and Chergui, K. (2020). NMDA receptors are altered in the substantia nigra pars reticulata and their blockade ameliorates motor deficits in experimental parkinsonism. Neuropharmacology *174*, 108136. https://doi.org/10.1016/j.neuropharm.2020.108136.

68. Baufreton, J., Atherton, J.F., Surmeier, D.J., and Bevan, M.D. (2005). Enhancement of excitatory synaptic integration by GABAergic inhibition in the subthalamic nucleus. J. Neurosci. *25*, 8505–8517. https://doi.org/10.1523/JNEUROSCI.1163-05.2005.

69. Hammond, C., Bergman, H., and Brown, P. (2007). Pathological synchronization in Parkinson's disease: networks, models and treatments. Trends Neurosci. *30*, 357–364. https://doi.org/10.1016/j.tins.2007.05.004.

70. Neumann, W.J., Degen, K., Schneider, G.H., Brücke, C., Huebl, J., Brown, P., and Kühn, A.A. (2016). Subthalamic synchronized oscillatory activity correlates with motor impairment in patients with Parkinson's disease. Mov. Disord. *31*, 1748–1751. https://doi.org/10.1002/mds.26759.

71. Belova, E.M., Filyushkina, V.I., Dzhalagoniia, I., Gamaleya, A.A., Tomskiy, A.A., Neumann, W.J., and Sedov, A. (2022). Oscillations of pause-burst neurons in the STN correlate with the severity of motor signs in Parkinson's disease. Exp. Neurol. *356*, 114155. https://doi.org/10.1016/j.expneurol.2022.114155.

72. Turner, R.S., and Desmurget, M. (2010). Basal ganglia contributions to motor control: A vigorous tutor. Curr. Opin. Neurobiol. *20*, 704–716. https://doi.org/10.1016/j.conb.2010.08.022.

73. Sutton, A.C., Yu, W., Calos, M.E., Smith, A.B., Ramirez-Zamora, A., Molho, E.S., Pilitsis, J.G., Brotchie, J.M., and Shin, D.S. (2013). Deep brain stimulation of the substantia nigra pars reticulata improves forelimb akinesia in the hemiparkinsonian rat. J. Neurophysiol. *109*, 363–374. https://doi.org/10.1152/jn.00311.2012.

74. Heilbronn, M., Scholten, M., Schlenstedt, C., Mancini, M., Schöllmann, A., Cebi, I., Pötter-Nerger, M., Gharabaghi, A., and Weiss, D. (2019). Anticipatory postural adjustments are modulated by substantia nigra stimulation in people with Parkinson's disease and freezing of gait. Park. Relat. Disord. *66*, 34–39. https://doi.org/10.1016/j.parkreldis.2019.06.023.

75. Shi, L.H., Luo, F., Woodward, D., and Chang, J.Y. (2006). Deep brain stimulation of the substantia nigra pars reticulata exerts long lasting suppression of amygdala-kindled seizures. Brain Res. *1090*, 202–207. https://doi.org/10.1016/j.brainres.2006.03.050.

76. Baumgartner, A.J., Thompson, J.A., Kern, D.S., and Ojemann, S.G. (2022). Novel targets in deep brain stimulation for movement disorders. Neurosurg. Rev. *45*, 2593–2613. https://doi.org/10.1007/s10143-022-01770-y.

77. Chastan, N., Westby, G.W.M., Yelnik, J., Bardinet, E., Do, M.C., Agid, Y., and Welter, M.L. (2009). Effects of nigral stimulation on locomotion and postural stability in patients with Parkinson's disease. Brain *132*, 172–184. https://doi.org/10.1093/brain/awn294.

78. Weiss, D., Wächter, T., Meisner, C., Fritz, M., Gharabaghi, A., Plewnia, C., Breit, S., and Krüger, R. (2011). Combined STN/SNr-DBS for the treatment of refractory gait disturbances in Parkinson's disease: study protocol for a randomized controlled trial. Trials *12*, 222. https://doi.org/10.1186/1745-6215-12-222.

79. Weiss, D., Walach, M., Meisner, C., Fritz, M., Scholten, M., Breit, S., Plewnia, C., Bender, B., Gharabaghi, A., Wächter, T., and Krüger, R. (2013). Nigral stimulation for resistant axial motor impairment in Parkinson's disease? A randomized controlled trial. Brain *136*, 2098–2108. https://doi.org/10.1093/brain/awt122.

80. Franklin, and Paxinos. (1997). The Mouse Brain in Stereotaxic Coordinates (Academic Press). https://doi.org/10.1111/j.1469-7580.2004.00264.x.

81. Abdi, A., Mallet, N., Mohamed, F.Y., Sharott, A., Dodson, P.D., Nakamura, K.C., Suri, S., Avery, S.V., Larvin, J.T., Garas, F.N., et al. (2015). Prototypic and arkypallidal neurons in the dopamine-intact external globus pallidus. J. Neurosci. *35*, 6667–6688. https://doi.org/10.1523/JNEUROSCI.4662-14.2015.

82. Cenci, M.A., and Lundblad, M. (2007). Ratings of L -DOPA-Induced Dyskinesia in the Unilateral 6-OHDA Lesion Model of Parkinson's Disease in Rats and Mice. Curr. Protoc. Neurosci. *41*, 9.25.1–9.25.23. https://doi.org/10.1002/0471142301.ns0925s41.

83. Chazalon, M., Paredes-Rodriguez, E., Morin, S., Martinez, A., Cristóvão-Ferreira, S., Vaz, S., Sebastiao, A., Panatier, A., Boué-Grabot, E., Miguelez, C., and Baufreton, J. (2018). GAT-3 Dysfunction Generates Tonic Inhibition in External Globus Pallidus Neurons in Parkinsonian Rodents. Cell Rep. *23*, 1678–1690. https://doi.org/10.1016/j.celrep.2018.04.014.

84. Mathis, A., Mamidanna, P., Cury, K.M., Abe, T., Murthy, V.N., Mathis, M.W., and Bethge, M. (2018). DeepLabCut: markerless pose estimation of user-defined body parts with deep learning. Nat. Neurosci. *21*, 1281–1289. https://doi.org/10.1038/s41593-018-0209-y.

85. Baufreton, J., and Bevan, M.D. (2008). D2-like dopamine receptor-mediated modulation of activity-dependent plasticity at GABAergic synapses in the subthalamic nucleus. J. Physiol. *586*, 2121–2142. https://doi.org/10.1113/jphysiol.2008.151118.

86. Holt, G.R., Softky, W.R., Koch, C., and Douglas, R.J. (1996). Comparison of discharge variability in vitro and in vivo in cat visual cortex neurons. J. Neurophysiol. *75*, 1806–1814. https://doi.org/10.1152/jn.1996.75.5.1806.

87. Legéndy, C.R., and Salcman, M. (1985). Bursts and recurrences of bursts in the spike trains of spontaneously active striate cortex neurons. J. Neurophysiol. *53*, 926–939. https://doi.org/10.1152/jn.1985.53.4.926.

88. Pasquale, V., and Martinoia, S. (2010). A self-adapting approach for the detection of bursts and network bursts in neuronal cultures. J. Comput. Neurosci. *2010*, 213–229. https://doi.org/10.1007/s10827-009-0175-1.

Please cite this article in press as: Delgado-Zabalza et al., Targeting parvalbumin-expressing neurons in the substantia nigra pars reticulata restores motor function in parkinsonian mice, Cell Reports (2023), https://doi.org/10.1016/j.celrep.2023.113287

STAR★METHODS

KEY RESOURCES TABLE

REAGENT or RESOURCE	SOURCE	IDENTIFIER
Antibodies		
Guinea Pig anti-NeuN antibody	Synaptic Systems	CAT#266 004 RRID: AB_2619988
Rat anti-RFP antibody	Chromotek	CAT#5f8; RRID: AB_2336064
Goat anti-PV antibody	Frontier Institute	CAT#Af460, RRID: AB_2571558
Rabbit anti-TH antibody	Novus	CAT#NB100-92231 RRID: AB_1218296
Rabbit anti-GFP antibody	Life Technologies	CAT#A11122; RRID: AB_221569
Alexa Fluor 488 Donkey anti-Rabbit	Life Technologies	CAT#A21206; RRID: AB_2535792
Alexa Fluor 488 Donkey anti-Goat	Jackson Immunoresearch	CAT#705-545-003 RRID: AB_2340428
Alexa Fluor 488 Donkey anti-Rat	Jackson Immunoresearch	CAT#712-545-150 RRID: AB_2340683
Alexa Fluor 594 Donkey anti-Guinea Pig	Jackson Immunoresearch	CAT#706-586-148; RRID: AB_2340475
Alexa Fluor 594 Donkey anti-Rat	Jackson Immunoresearch	CAT# 712-585-153; RRID: AB_2340689
Alexa Fluor 647 Donkey anti-Rabbit	Jackson Immunoresearch	CAT# 711-605-152; RRID: AB_2492288
Biotin-SP Donkey Anti-Rabbit IgG	Jackson Immunoresearch	CAT#711-065-152
Bacterial and Virus Strains		
AAV8-hSyn-DIO-HA-hM4D(Gi)-IRES-mCitrine	Bryan Roth Lab	Addgene # 50455; RRID: 50455
AAV8-hSyn-DIO-HA-hM3D(Gq)-IRES-mCitrine	Bryan Roth Lab	Addgene # 50454; RRID: 50454
AAV5-EF1α-DIO-ChR2(H134R)-EYFP	University of North Carolina at Chapel Hill Vector Core (UNC)	Lot#AV4313P
AAV5-EF1α-DIO-ChR2(H134R)-mCherry	University of North Carolina at Chapel Hill Vector Core (UNC)	Lot#AV4385E
AAV5-EF1a-DIO-EYFP	Karl Deisseroth Lab	Addgene # 27056; RRID:Addgene_27056
Chemicals, Peptides, and Recombinant Proteins		
Isoflurane	Piramal Healthcare UK Limited	Iso-vet®; CAT: 26675-46-7
Lidocaine	Aspen	Emla cream®; CAT:N01B B20
Ophthalmic ointment (ster)	Bauch & Lomb Swiss	liposic®
D-(+)-Glucose	Sigma-Aldrich	CAT#G8270; CAT: 50-99-7
Buprenorphine	Virbac	Bupaq®; CAT#: QN02AE01
Meloxicam	Virbac	Inflacam®; CAT#: QM01AC06
Biocytin	Sigma-Aldrich	CAT#B4261
Hydrogen peroxide solution	Sigma-Aldrich	CAT#H1009
Normal Goat Serum	Sigma-Aldrich	CAT#G9023 RRID: SLCH5798
Bovine Serum Albumin	Sigma-Aldrich	CAT#A9418
ABC Kits	Vector laboratories	VECTASTAIN®; CAT:PK-6100
DAB Substrate Kit with Nickel	Vector laboratories	CAT:SK-4100
Vectashield medium	Vector laboratories	CAT#H-1000
DAPI Fluoromount-G	SouthernBiotech	CAT#0100-20
Fluoromount-G	SouthernBiotech	CAT#0100-01

(*Continued on next page*)

Please cite this article in press as: Delgado-Zabalza et al., Targeting parvalbumin-expressing neurons in the substantia nigra pars reticulata restores motor function in parkinsonian mice, Cell Reports (2023), https://doi.org/10.1016/j.celrep.2023.113287

Continued

REAGENT or RESOURCE	SOURCE	IDENTIFIER
EUKITT	Orsatec	N/A
Triton™ X100	Sigma-Aldrich	CAT#T9284
QX-314 hydrobromide	Bio-Techne	CAT#1014
DNQX disodium salt	Bio-Techne	CAT#2312
CGP 55845 hydrochloride	Bio-Techne	CAT#1248
D-AP5	Bio-Techne	CAT#0106
ZD 7288	Bio-Techne	CAT#1000
6-Hydroxydopamine hydrobromide	Bio-Techne	CAT#2507
Desipramine hydrochloride	Bio-Techne	CAT#3067
Clozapine-N-oxide	Bio-Techne	CAT#4936
Pyr3	Bio-Techne	CAT#3751
SR 95531 hydrobromide	Bio-Techne	CAT#1262
L-703,606 oxalate salt hydrate	Sigma-Aldrich	CAT#119
N-Methyl-D-glucamine	Sigma-Aldrich	CAT# M2004
Alexa Fluor 647 Streptavidin	Life Technologies	CAT#: S21374 RRID: AB2336066
Alexa Fluor 488 Streptavidin	Life Technologies	CAT#: S11223
Experimental Models: Organisms/Strains		
Mouse: PVcre::Ai9T (PV-IRES-Cre; Rosa26$^{lsl\text{-}tdTomato}$; Ai9T)	University of Bordeaux Animal facility (CRYME)	N/A
Software and Algorithms		
Multiclamp 700B	Molecular Devices	RRID:SCR_018455
Digidata 1550B	Molecular Devices	RRID: N/A
Graphpad Prism 8 (version 8.4.3)	Graphpad software Inc	RRID:SCR_002798
Fiji	http://fiji.sc	RRID:SCR_002285
Adobe Illustrator	Adobe Systems	RRID:SCR_014198
pClamp 10 (version 10.3 & 10.6)	Molecular Devices	RRID:SCR_011323
Origin	MicroCal Origin	RRID:SCR_002815
DeepLabCut	DeepLabCut™	https://github.com/DeepLabCut/DeepLabCut
NDP view 2	Hamamatsu	CAT#SBIS0066E
Other		
Vibratome VT1200S	Leica Microsystems	RRID:SCR_018453
Pneumatic PicoPump	World Precision Instruments	CAT#: SYS-PV820
Microcapillary pipette	Sigma-Aldrich	Hirschmann® CAT#: Z611239
Silicone elastomer	Elkem	Silbione RTV4420

RESOURCE AVAILABILITY

Lead contact

Further information and requests for resources and reagents should be directed to and will be fulfilled by the lead contact, Jérôme Baufreton (jerome.baufreton@u-bordeaux.fr).

Materials availability

This study did not generate new unique reagents.

Data and code availability

- All data reported in this manuscript will be shared upon request from the lead contact.
- This paper does not report original code

- Any additional information required to reanalyze the data reported in this work paper is available from the lead contact upon request.

EXPERIMENTAL MODEL AND SUBJECT DETAILS

All procedures comply with the ARRIVE guidelines and were performed in accordance with the EU Directive 2010/63/EU. Experimental protocols were approved by the local ethical committee and the French and Spanish Ministry of Research A5012075, APAFIS#14255 and M20-2017-006. Male and female 8- to 12- week old PVcreAi9T (PV^{i-Cre}, JAX #008069; $Rosa26^{lsl\text{-}tdTomato}$, JAX #007909) transgenic mice were used for the experiments. Animals were housed under a 12:12 light-dark cycle with food and water provided *ad libitum*. All efforts were made to minimize animal suffering and to reduce the number of animals used.

METHOD DETAILS

Histology

Adult mice (8-12 weeks old, 25-30g) were deeply anesthetized with a mixture of ketamine and xylazine (75 mg/kg and 10 mg/kg, respectively, i.p.), killed and perfused transcardially with ice-cold modified artificial cerebrospinal fluid (ACSF), equilibrated with 95% O_2 and 5% CO_2, and containing (in mM): 230 sucrose, 26 $NaHCO_3$, 2.5 KCl, 1.25 NaH_2PO_4, 0.5 $CaCl_2$, 10 $MgSO_4$ and 10 glucose. Brains were post-fixed overnight in a solution of 4% w/v PFA in 0.1 M phosphate buffered saline, pH 7.4 (PBS) at 4°C. The day after PFA was removed and brains were stored in PBS-azide 0.2% before being cut into 50 μm coronal sections on a vibratome (VT1000S; Leica Microsystems).

Quantification of molecular marker expression in populations of SNr neurons

50 μm-thick free-floating coronal tissue sections were collected in series, washed in PBS, and those containing "rostral", "central," and "caudal" SNr were selected. A total of 22 slices from 6 mice and both hemispheres were used. According to the adult mouse brain atlas these sections, respectively, correspond to approximate distances of 2.8, 3.0, and 3.2 mm posterior to bregma.[80] They were then processed for indirect immunofluorescence to reveal molecular markers.[81] Briefly, sections were washed six times for 5 min in PBS then incubated for 1 h at room temperature in a blocking solution of PBS containing 10% Normal Goat Serum (NGS; Sigma-Aldrich) and 0.3% Triton X-100 (Sigma-Aldrich). Slices were incubated overnight with a mixture of between two and three of the following primary antibodies: anti-red fluorescent protein (RFP; 1:1000 dilution; ChromoTeck), anti-Green Fluorescent Protein (GFP; 1:1000 dilution; Life Technologies), anti-neuronal nuclear protein (NeuN; 1:2000 dilution; Synaptic Systems) and anti-tyrosine hydroxylase (TH; 1:1000 dilution; Novus) or anti-Parvalbumin (PV; 1:1000 dilution; Frontier Institute). After exposure to primary antibodies, sections were washed in PBS and incubated at room temperature for 90 min in blocking solution containing a cocktail of secondary antibodies (all raised in donkey) conjugated to the following fluorophores: Alexa Fluor 488 (1:500 dilution; Jackson Immunoresearch); Alexa Fluor 568 (1:500 dilution; Jackson Immunoresearch); or Alexa Fluor 647 (1:500 dilution; Jackson Immunoresearch). Sections were then rinsed in PBS, mounted on gelatin-coated slides, and coverslipped in Vectashield (Vector Laboratories). For anterograde tracing experiments, slides were counter stained in DAPI Fluoromount medium (SouthernBiotech).

Tyrosine hydroxylase immunostaining

After the inactivation of endogenous peroxidases sections were incubated for 60 min in PBS containing 10% NGS and 0.3% Triton X-100. Next, slices were incubated in primary antibody anti-TH (1:1000; Novus) overnight in gentle agitation at room temperature. The day after, sections were washed in PBS and incubated with the secondary antibody (biotinylated donkey anti-rabbit IgG; 1:1000 dilution; Vector Laboratories) for 90 min at room temperature. Both immunoreagents were diluted in PBS containing 10% NGS and 0.3% Triton X-100. Finally, sections were incubated in avidin-biotin peroxidase complex (1:500 dilution; Vector Laboratories) for 60 min and immunoreactivity was revealed using 3,3′-diaminobenzidine tetrahydrochloride hydrate (DAB) peroxidase substrate kit (Vector Laboratories). Following DAB staining, sections were rinsed (6 × 5 min) and dehydrated following the next sequence in seconds; 90% ethanol (30 s); 90% ethanol (30 s); 100% ethanol (30 s); 100% ethanol (30 s); xylene (30–60 s), mounted on gelatin-coated slides, and coverslipped in EUKITT mounting medium (Sigma-Aldrich). The entire procedure was performed at room temperature under gentle agitation.

Imaging and anatomical analyses

Epifluorescent acquisitions (Carl Zeiss, AxioImager.M2) were performed using Morpho Strider software (Carl Zeiss). For imaging the three fluorescence channels, we employed the following filter cubes: Alexa Fluor 488, Cy3 532 and DyLight 649. Images of each of the channels were taken sequentially and separately to negate possible crosstalk of signal across channels. We first used a 5 X 0.16 NA objective lens to perform coronal mosaic images, subsequently, 20× 0.16 NA objective was used to capture our interest region, the SNr. The medial and lateral borders of the SNr were readily delineated according to TH staining. We carried out the counting over the entire SNr in both hemispheres, on sections at the designated rostral, central, and caudal levels. To minimize confounds and ensure accurate cell counts, we used confocal images obtained from a BX51 Olympus Fluoview 500 microscope using an oil-immersion 20×

Please cite this article in press as: Delgado-Zabalza et al., Targeting parvalbumin-expressing neurons in the substantia nigra pars reticulata restores motor function in parkinsonian mice, Cell Reports (2023), https://doi.org/10.1016/j.celrep.2023.113287

objective 0.8 numerical aperture. Laser light sources were an Argon laser, a Helium-Neon (green) laser, and Helium-Neon (red) laser. Neuron counting and neuronal marker co-localization were achieved using the "cell-counter" plug-in of ImageJ by two independent investigators. Data from rostral, central, and caudal SNr of both hemispheres were pooled for further analyses.

To quantify SNr axon terminals density for whole brain mapping projectome of SNr-PV+ neurons, FITC, TRITC and DAPI channels were read into a slide's scanner (Hamamatsu NANOZOOMER 2.0HT). The software NDP2 viewer was used to establish the brightness/contrast settings per mouse. Then, images were exported and opened in ImageJ, where they were converted to 8-bit gray scale tiff file. As the most densely innervated target is the ventro-medial (VM) motor thalamus, structure boundary ROIs were defined according to criteria in a standard atlas.[80] HILO tool was employed to define the best correlation brightness/contrast for the background in order to avoid saturation. These settings were adjusted for each mouse (n = 3). The percentage of optical density was calculated by subtracting the density par region multiplied by 100 and divided by the total density of all brain structures targeted by SNr-PV+ neurons.

For quantification of DREADD-mCitrine+ and tdTomato+ co-localization in SNr neurons, confocal stacks (10–30 μm in z) were obtained from sagittal sections throughout the entire medial-lateral axis of the SNr. The percentage of mCitrine and tdTomato co-localization was assessed by dividing the number of mCitrine+/tdTomato+ SNr neurons by the total number of mCitrine neurons. We excluded 2 mice in which DREADDs expression extended beyond the target nuclei or if off target expression was higher than 20%.

Tyrosine hydroxylase optical density

Optical density was used to measure the percentage of dopamine depletion. At least two sections from each hemisphere containing the STR were scanned (Microscope Slide Scanner, Leica Biosystems) and further processed (ViewScan). Mean optical density was measured on the STR from the contralateral and ipsilateral slices to the lesion and analyzed using the tool "Set Measurements" from ImageJ software. Values were corrected for background staining (measured in the cortex above the STR). TH optical density levels were expressed as the mean percentage of the values from the ipsilateral side with respect to the contralateral non-lesioned side. Animals with unilateral 6-OHDA infusions included in the study showed >80% reduction in TH-fiber density in the STR on the ipsilateral side to the lesion (Figure S6).

Behavioral assessment

Two behavioral tests, namely the cylinder and the open field tests, were used to measure the degree of motor impairment induced by the 6-OHDA lesion. Subsequently, chemogenetic approaches were used to assess the effect of manipulating SNr-PV+ neurons on motor performances. For that, either Clozapine-N-Oxyde (CNO; 2 mg/kg) or normal saline (0.9% NaCl) were administered i.p. in a random order and spaced at least 24h apart. The dose of CNO was chosen based on the dose-response curve on rotations in 6-OHDA mice established recently.[48] Behavioral tests were performed 30 min after i.p. drug administration. CNO solution was prepared in opaque Eppendorf tubes covered with aluminum foil for avoiding oxidation.

Cylinder test

To assess the degree of motor impairment, we evaluated forelimb use asymmetry in the cylinder test.[82,83] Briefly, mice were placed individually in a 1000 mL cylindrical glass beaker (10.7 cm diameter; 14,5 cm height; Fisherbrand) located in front of two vertical mirrors in order to observe the mice from all angles, and allowed to move freely for 5 min. Mice were video-recorded using a 4K Ultra HD DV 12MP 1080p 60fps camera and analyzed offline. Forelimb placements on the walls of the beaker were counted manually during video review. Data were expressed as a percentage of use of the contralateral forelimb ([contralateral paw placements/(ipsilateral + contralateral paw placements)] ×100); (Figures S7A–S7C).

Open field

Mice were placed in the center of a 40 × 40 × 40 cm open top box and allowed to freely move about for 15 min while being recorded by a video camera located above the box (30 fps). Between animals, arena was cleaned with 70% ethyl alcohol and dry. In order to reduce effects of habituation, testing was performed at least 2 days apart. Each mouse was tested in the open field two times (after CNO and saline injections). The total distance traveled in the open field was obtained from a frame-by-frame analysis of 5 body landmarks previously defined (tail end, tail base, mid-body, head and nose). By using the mid-body X-Y coordinates obtained from Deep Lab Cut,[84] we employed the Pythagorean theorem in order to find the distance between any two points. Before further processing the data, we checked for errors in the result and corrected by excluding values that exceeded 2 times the mean. The velocity was obtained by averaging the distance values per frame. The number of 360-degree turns were counted manually regarding the 15 min video in open field test (Figures S7D and S7E). Cylinder and open-field video scoring were perform by an independent experimenter blind to the experimental condition.

Animal surgery

Unilateral 6-OHDA injections

Male and female mice (postnatal 6–10 weeks) were anesthetized with 5% vaporized isofluorane (Tem-Sega Inc. Pessac) and placed in a stereotaxic frame with a mouse-adaptor (David Kopf Instruments with Digital Display Console). 6-hydroxydopamine (6-OHDA) (dissolved in 0.02% ascorbic acid) was injected into the right medial forebrain bundle (MFB) at a rate of 0.5 μL/min by using a glass

Please cite this article in press as: Delgado-Zabalza et al., Targeting parvalbumin-expressing neurons in the substantia nigra pars reticulata restores motor function in parkinsonian mice, Cell Reports (2023), https://doi.org/10.1016/j.celrep.2023.113287

micropipette connected to a Picopump. We injected 1 μL of 6-OHDA (3.2 μg/μL) at the following coordinates: AP: −1.3 mm, ML: −1.2 mm, DV: −4.75 mm (relative to bregma, sagittal suture and dural surface, cf.[80] After each injection, the needle was left in place for an additional 2–4 min to allow the toxin to diffuse into the structure and avoid backflow before being slowly retracted. Analgesia was achieved by subcutaneous (s.c.) injection of 0.05 mL/10 g body weight, of Rimadyl (Carprofen, 250 mg/kg). In order to prevent the damage of noradrenergic neurons, mice were pretreated, approximately 25 min before the injection of 6-OHDA, with desipramine (25 mg/kg, i.p; Sigma-Aldrich). Sham injection was carried out by 1 μL injection of 0.02% ascorbic acid-saline at the same coordinates. To prevent dehydration mice received sterile glucose–saline 20% (0.1 mL/10 g body weight, s.c.) immediately after surgery and once a day during the first post-operative week. In addition, during the first 4–5 days or until they stop losing weight, mice received Rimadyl (0.05 mL/10 g body weight, s.c.) in the morning. Then we replaced this nonsteroidal anti-inflammatory drug (Rimadyl) by saline injections (0.9% NaCl, 0.5 mL/20 g body weight, s.c) during the following days.

Viral vector injections

All the virus used for our optogenetic and chemocogenetic manipulations were adeno-associated virus directly purchased from a vector core (UNC vector core) and micro-injected under stereotaxic condition in PVcreAi9T mice using glass capillary (tip diameter 35 μm; 1–5 μL) connected to a Picopump. Briefly, mice were anesthetized with isoflurane (induction/maintenance: 3–5/1.5%; Iso-vet, Piramal healthcare), fixed on a stereotaxic frame (Unimécanique, M2e) and placed on a heating blanket. An ophthalmic ointment (Liposic, Bauch & Lomb Swiss) was used all along the surgery to prevent dehydration. For anterograde tracing experiments a craniotomy (0.5–1 mm diameter) was made in PVcreAi9T and a AAV5-EF1a-DIO-ChR2 (H134R)-EYFP viral vector ($4x10^{12}$ viral particles/mL) was injected unilaterally in the SNr at the following coordinates, AP -3.3 mm, ML - 1,6, DV -4.7 mm, volume: 60 nL). Photo-stimulation (opto-tagging) of SNr-PV+ neurons was performed using the same adeno associated virus at the same SNr coordinates aforementioned. For the *in vivo* validation of CNO effect on SNr-PV+ cells, AAV5-EF1a-DIO-ChR2(H134R)-mCherry ($5.3x10^{12}$ viral particles/mL) and AAV8-hSyn-DIO-HA-hM4D(Gi)-IRES-mCitrine ($2.4x10^{13}$ viral gemone/mL) viral vectors were injected into the SNr of PVcreAi9T mice at the same coordinates previously mentioned.

For the behavioral experiments, chemogenetic excitation and inhibition experiments were performed in PVcreAi9T animals that were injected unilaterally into the SNr using AAV8-hSyn-DIO-HA-hM4D(Gi)-IRES-mCitrine ($2.4x10^{13}$ viral gemone/mL) or AAV8-hSyn-DIO-HA-hM4D(Gi)-IRES-mCitrine ($3x10^{13}$ viral gemone/mL) vectors at similar coordinates and volume as aforementioned. To control for a non-specific effect on locomotion, we additionally performed pharmaco-genetic experiments in animals injected unilaterally in the SNr with the control virus AAV5-EF1α-DIO-eYFP ($6.5x10^{12}$ viral particles/mL).

Ex vivo electrophysiology procedures

Slice preparation. Animals were anesthetized with a mixture of ketamine and xylazine (75 mg/kg and 10 mg/kg, respectively, i.p.) and transcardially perfused with ice-cold modified artificial cerebrospinal fluid (ACSF), equilibrated with 95% O_2 and 5% CO_2, and containing (in mM): 230 sucrose, 26 $NaHCO_3$, 2.5 KCl, 1.25 NaH_2PO_4, 0.5 $CaCl_2$, 10 $MgSO_4$ and 10 glucose. Brains were then quickly removed from the skull, blocked in the parasagittal or coronal plane, glued to the stage of a vibratome (VT1200S; Leica Microsystems, Germany) and sectioned into 300 μm-thick parasagittal slices. Slices containing the SNr were then left to equilibrate for ∼1 h (at ∼35°C) in ACSF of the following composition (in mM): 126 NaCl, 26 $NaHCO_3$, 2.5 KCl, 1.25 NaH_2PO_4, 2 $CaCl_2$, 2 $MgSO_4$, 10 glucose, 1 sodium pyruvate and 4.9 L-gluthathione reduced (gassed with 95% O2–5%). Then, slices were kept at room temperature (22°C–26°C) in oxygenated ACSF until transfer to the recording chamber.

Electrophysiological recordings

Single slices were transferred to a recording chamber, perfused continuously with a recording solution of the following composition (in mM): 126 NaCl, 26 NaHCO3, 1.25 NaH2PO4, 3 KCl, 1.5 MgSO4, and 1.6 CaCl2 and 10 glucose, then visualized using infrared gradient contrast video microscopy (E600FN, Eclipse workstation, Nikon, Japan) and a water-immersion objective (Nikon Fluor 60×/1.0 NA). Low sodium solution voltage clamp experiments were performed using extracellular solutions in which 125 mM NaCl was replaced by NMDG. Solutions were made by first adding (in mM) 125 NMDG, 25 $NaHCO_3$ and 1.25 NaH_2PO_4 to the beaker. Next, the NMDG solution was titrated with HCl to a pH of 7.3–7.4. We then added 10 glucose and then bubbled the solution with 95/5% O_2/CO_2 to saturation. Last, either 1 $MgCl_2$ alone or 1 $MgCl_2$ plus 2 $CaCl_2$ were added.the same extracellular solutions.[60] The microscope was also equipped with epifluorescence (Nikon Intensilight C-HGFI) that allowed us to perform selective patch-clamp targeting of PV-expressing or PV non-expressing SNr neurons in real time. Recordings were obtained using a Multiclamp 700B amplifier and Digidata 1550B digitizer controlled by Clampex 10.6 (Molecular Devices, Sunnyvale, CA, USA). Recordings from individual neurons were made using pipettes (impedance, 3–6MΩ) prepared from borosilicate glass capillaries (G150–4; Warner Instruments, Hamden, CT, USA) with a micropipette puller (P- 97; Sutter Instruments, Novato, CA, USA). In whole cell voltage-clamp recordings, cells were held at −60 mV and series resistance (Rs) was monitored by a step of −5 mV. Data were discarded if Rs exceeded 25 MΩ or when the series resistance changed ±20%. Signals were low-pass filtered at 2 kHz and sampled at 10 kHz for voltage clamp mode, and at 4 kHz and sampled at 20 kHz for current clamp mode. In experiments designed to define the autonomous and driven firing of the SNr, neurons were first recorded in cell-attached mode and then in whole-cell current-clamp mode. The patch pipette solution contained (in mM): 135 K-gluconate, 3.8 NaCl, 1 $MgCl_2.6H_2O$, 10 HEPES, 0.1 EGTA, 0.4 Na_2GTP, 2 $Mg_{1.5}ATP$, 5 QX-314 and 5.4 biocytin (pH = 7.2, ∼292 mOsm). The pH and osmolarity of the pipette solution were adjusted at 7.2 and 290 mOsm l^{-1}, respectively. In cell-attached configuration SNr neurons were recorded for 2–4 min at a holding potential of 0 mV after the stable establishment of the gigaseal. Once completed, the holding potential was set at −60 mV to switch in whole-cell configuration and the spontaneous

firing of SNr neurons was recorded in current-clamp mode. Negative and positive steps of currents were injected through the patch-pipette to collect membrane properties and driven activity of SNr neurons. All recordings were achieved in the presence of NMDA and AMPA glutamatergic receptor antagonists (50 μM D-AP5, 20 μM DNQX, respectively) and GABAergic synaptic transmission (50 μM picrotoxin). The junction potential (13mV; JPCalc, Clampex 10) was not corrected.

In vivo electrophysiology procedures

Electrophysiological recordings and optogenetic manipulations were realized at least 3 weeks after viral transduction under isoflurane anesthesia (1–2.5%; Iso-vet, Piramal healthcare). The animals were then secured in a stereotaxic frame (Unimécanique, M2e) and placed on a heating blanket. After subcutaneous injection of xylocain, the skull was exposed and craniotomies were performed to enable electrophysiological recordings and optogenetic stimulation of the region of interest (same stereotaxic coordinates as above). In each mouse, an electrocorticogram (ECoG) of the sensorimotor cortex was realized (AP: 2.2 mm rostral to bregma, ML: 2.1 mm) with a 1 mm screw juxtaposed to the dura mater. This ECoG signal was referenced toward another 1mm screw implanted above the cerebellum and both screws were covered with silicone elastomer (Elkem, Silbione RTV4420). All along the recording session, saline solution was used to prevent dehydration and anesthesia level was frequently controlled by examination of EcoG.

In vivo extracellular recordings were performed using glass electrodes (1–3 μm tip end, 10-20MΩ, GC150F, WPI) filled with a chloride solution 0.5 M. Since a DIO-ChR2 virus was injected into the SNr of PV-Cre mice, we performed optotagging identification of SNr-PV+ neurons using a homemade opto-electrode that consisted of gluing an optical fiber (multimode Fiber, 0.22NA, core diameter: 105μm, Thorlabs) 1.2mm above the tip of the recording glass electrode. Brief pulses of blue (493nm) light stimulation were applied using the following light parameters; pulse duration: 10 ms, interval: 150 ms, repetition: >200 times, light intensity: 2.5–35 mW. Optotagged SNr neurons were identified as neurons responding with a short delay (<10 ms) to opto-excitatory stimulation. Once opto-electrode was implanted in the recording structure, the signal was amplified by 10-fold in AxoClamp 2B (in bridge mode; Molecular Devices). Then, recording signal was amplified 1000-fold and filtered with differential AC amplifier (spike unit: 0.3–10 kHz, local field potential: 0.1Hz-10 kHz; model 1700, A-M Systems). For ECoG recording, the signal was amplified 1000-fold and filtered with the same differential AC amplifier (0.1Hz-5 kHz). Finally, the recorded signals were digitized at 20 kHz, by using the Power1401-3 connected to a computer equipped with Spike2 software (version 8, Cambridge Electronic Design). Histological visualization of the track left by the electrode further confirm the recording location in the SNr.

In vivo local pharmacology

Injection pipettes were pulled from glass capillaries (Ringcaps@; Hirschmann Laborgerate) and the tip was broken under a microscope to reach an external diameter of around 30 μm. The injection pipette was then glued at 140–170 μm above the tip of the recording electrode. The injection pipette was then filled with a solution containing blockers of the ionotropic glutamatergic receptors, D-(−)-2-amino-5-phosphonopentanoic (AP5; 500 μM) and 6,7-dinitroquinoxaline-2,3-dione (DNQX; 200 μM), to block MNDA and AMPA/kainite, respectively. In some experiments, L703,606 (50 μM) a selective NALCN channels blocker was also injected *in vivo*. All drugs were diluted the day of the experiment in sodium chloride solution 0.9%. This solution was injected in the vicinity of the recorded neurons at a volume of 20–40 nL using air pressure within 20–40 s. Pressure injection often induced a mechanical effect that could induced a decrease in the spike amplitude. In most cases, the spike amplitude recovered spontaneously within 1 min. We discarded the first minute after injection to avoid changes in the activity of the recorded neurons induced by a mechanical effect. The effect of glutamatergic blockers on neuronal activity took place within 3–5 min following the injection and could last up to 20 min after the injection. As a result, the optimal time frame of the drug effect was determined on a 5-min window within these time epochs for each individual neuron by evaluating its firing response to the observed effect.

Data analysis and statistics

Ex vivo *recordings*

Membrane resistance (Rm) and capacitance (Cm) were calculated in whole-cell voltage-clamp configuration using a 5 mV step of potential (ΔV). Rm was determined using the Ohm's law (U = R.I) using the steady-state current at the end of the step of potential. Cm was calculated using the following formaula: Cm = Q/ΔV in which Q correspond to the area under the curve of the capacitive current that correspond to the total charge Q ($Q=\int I.dt$) accumulated on the membrane capacitor during the initial (capacitive) current transient after substraction of the steady state current. Action potential threshold (APth) was detected using a custom algorithm (available on request) that detected the first point of sustained positive ''acceleration'' of voltage [$(\delta V/\delta t)/\delta t$] and was also more than two times the SD of membrane noise before APth.[68] The rebound burst (Rb) was defined as the instantaneous frequency superior to the mean frequency ±3 SD.[85]

In vivo recordings

All data processing was realized offline with Spike2 software (Cambridge Electronic Design). Laser response of SNr neurons to the optotagging stimulation protocol were determined using peristimulus time histograms (PSTH) using spike2 custom script (width: 100 ms, offset: 50 ms, bin size: 1 ms). A neuron was classified optotagged and thus putative SNr-PV+ if the spike count values of 3 consecutive bins of light pulse were >2 standard deviation (SD). We also analyzed in spike2 the frequency, regularity of firing using

Please cite this article in press as: Delgado-Zabalza et al., Targeting parvalbumin-expressing neurons in the substantia nigra pars reticulata restores motor function in parkinsonian mice, Cell Reports (2023), https://doi.org/10.1016/j.celrep.2023.113287

mean CV2,[86] and the burst properties for each opto-tagged SNr-PV+ neuron. The bursts were detected using a Spike2 script based on the Poisson surprise method.[87] Briefly, this method determines how improbable any given burst containing *n* spikes in a time interval *T* occurred by chance. It is computed by $S = -log\ p$, where *p* is the probablitity that, in a random Poisson spike train with the same average spike rate *r* as the spike train studied, a given time interval of length *T* contains *n* or more spikes. *P* is given by the Poisson's formula as follows.Where S refers to the Poisson Surprise of the burst. In this work, only spike trains with $S \geq 2$ were considered to be burst. Analyses were carried out offline using Clampfit 10.6 (Molecular Devices), OriginPro 8.0 (Microcal Software) for *ex vivo* electrophysiology, spike2 for *in vivo* electrophysiology and ImageJ for image processing. Pause in the *in vivo* firing activity of SNr neurons were defined as log(ISI) > Mean log(ISI)+2SD.[88] For behavioral experiments we used DeepLabCut and the open source Python code to generate the diagrams of mice behavior in the open field test.

QUANTIFICATION AND STATISTICAL ANALYSIS

Electrophysiological data in the figures are presented using boxplots (central line: median; box: inter-quartile; whiskers: 10–90 data range) unless otherwise stated. Anatomy and behavioral data were presented using Mean ± S.E.M. Individual values are provided in all figures to illustrate sample distributions. Data in the text are presented as median ± median absolute deviation (M.A.D.) unless otherwise stated.

The statistical analysis was carried out with the computer program GraphPad Prism (v. 9.01, GraphPad Software, Inc). Differences in electrophysiological parameters were compared using the nonparametric Mann-Whitney U (MW-U) test for unpaired statistical comparisons. Wilcoxon signed rank (WSR) and Friedman's test (followed by Dunn's post-hoc test) were used for paired comparisons between two or more than two groups, respectively. p values smaller than 0.05 were considered statistically significant. For multiple groups comparisons and when data were normally distribution (shapiro-wilk test) two-way ANOVA with Sidak's post-hoc test was applied. In the text, the F and p values reported is the one from interaction.

Cell Reports, Volume ■ ■

Supplemental information

Targeting parvalbumin-expressing neurons in the substantia nigra pars reticulata restores motor function in parkinsonian mice

Lorena Delgado-Zabalza, Nicolas Mallet, Christelle Glangetas, Guillaume Dabee, Maurice Garret, Cristina Miguelez, and Jérôme Baufreton

Supplemental information

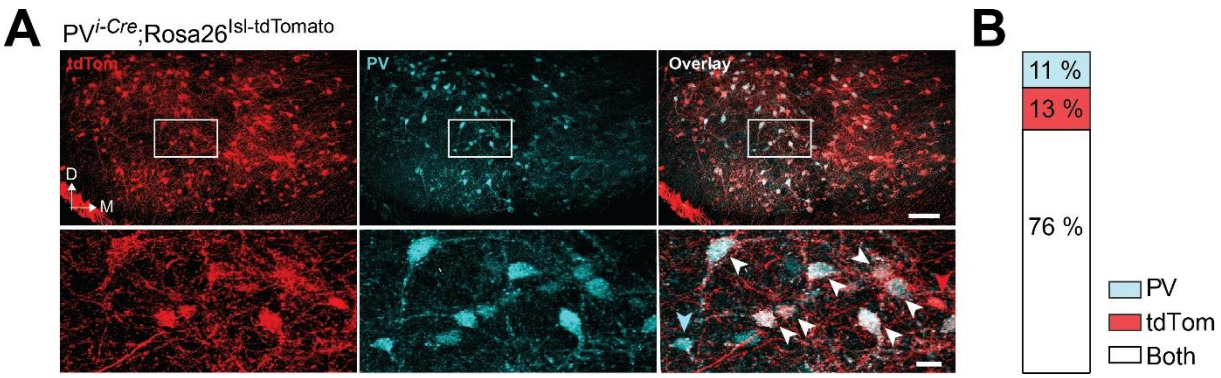

Figure S1. Distribution of tdTomato and PV immunoreactivity in SNr neurons. (Related to Figure 1).
A, top panels: coronal brain section of the SNr from a PVcre::Ai9T mouse where Cre expression is reported by tdTomato (**A**, *left panels;* red) followed by PV immunolabeling in cyan (**A**, *middle panels;* cyan). *Right*, co-localization between the two markers (**A**, *right panels*). Scale bar: 200μm. **A, bottom panels:** high magnification images of boxed areas showing the strong degree of co-localization between tdTomato and PV in SNr neurons (co-localization: white arrowheads; PV labelling only: blue arrowheads; tdTomato labelling only: red arrowhead). Scale bar: 30μm. **B:** Quantification of co-localization between tdTomato and PV in the SNr. Data were obtained from 6 mice and a total of 13 slices. See Table S3 for more details and statistical information.

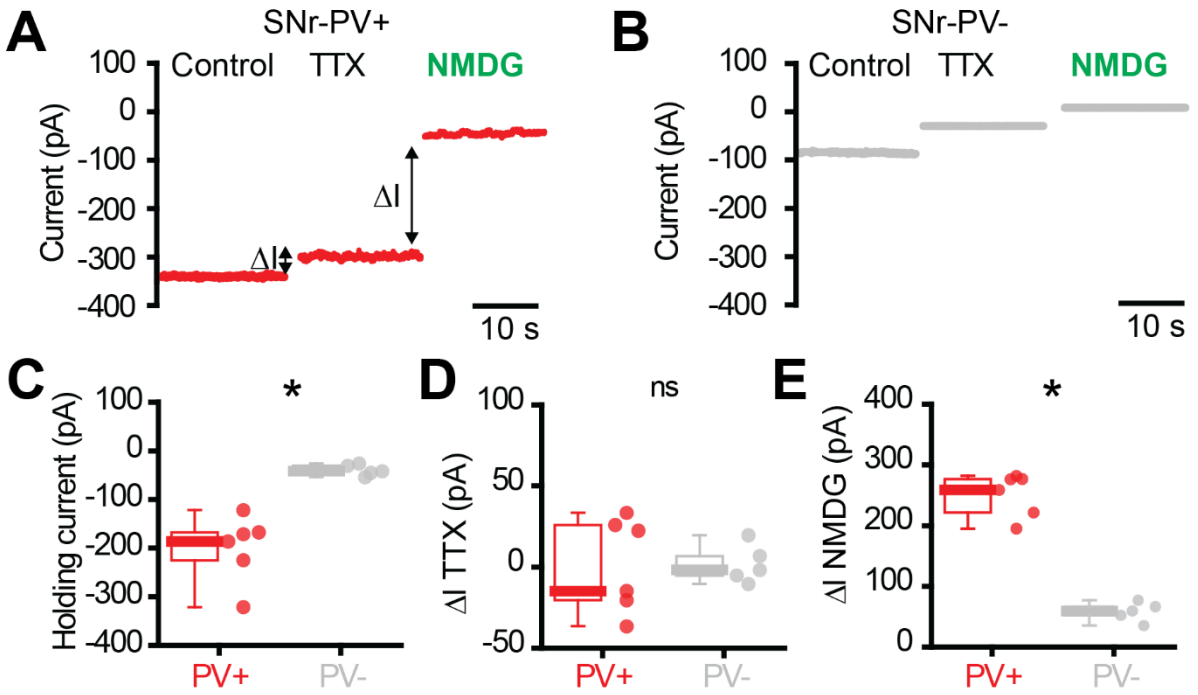

Figure S2: Differential expression of background sodium channels between SNr-PV+ and SNr-PV- neurons. (Related to figure 2).

A-B: Representative holding currents recorded under normal ACSF, in presence of TTX (1µM) and after extracellular sodium substitution by N-Methyl-D-Glucamine (NMDG) in a SNr-PV+ (**A**) and a SNr-PV- (**B**) neuron. **C-E**: Population graph showing the significant difference in holding current between SNr-PV+ and SNr-PV- neurons (**C**), the holding current shift induced by TTX (ΔI TTX); (**D**) and the holding current shift induced by sodium substitution (ΔI NMDG); (**E**) in SNr-PV+ (n=6) neurons compared to SNr-PV- (n=5) cells. Box-and-whisker plots indicate median, inter- quartile, and 10-90 range values. *p<0.05. See Table S3 for more details and statistical information.

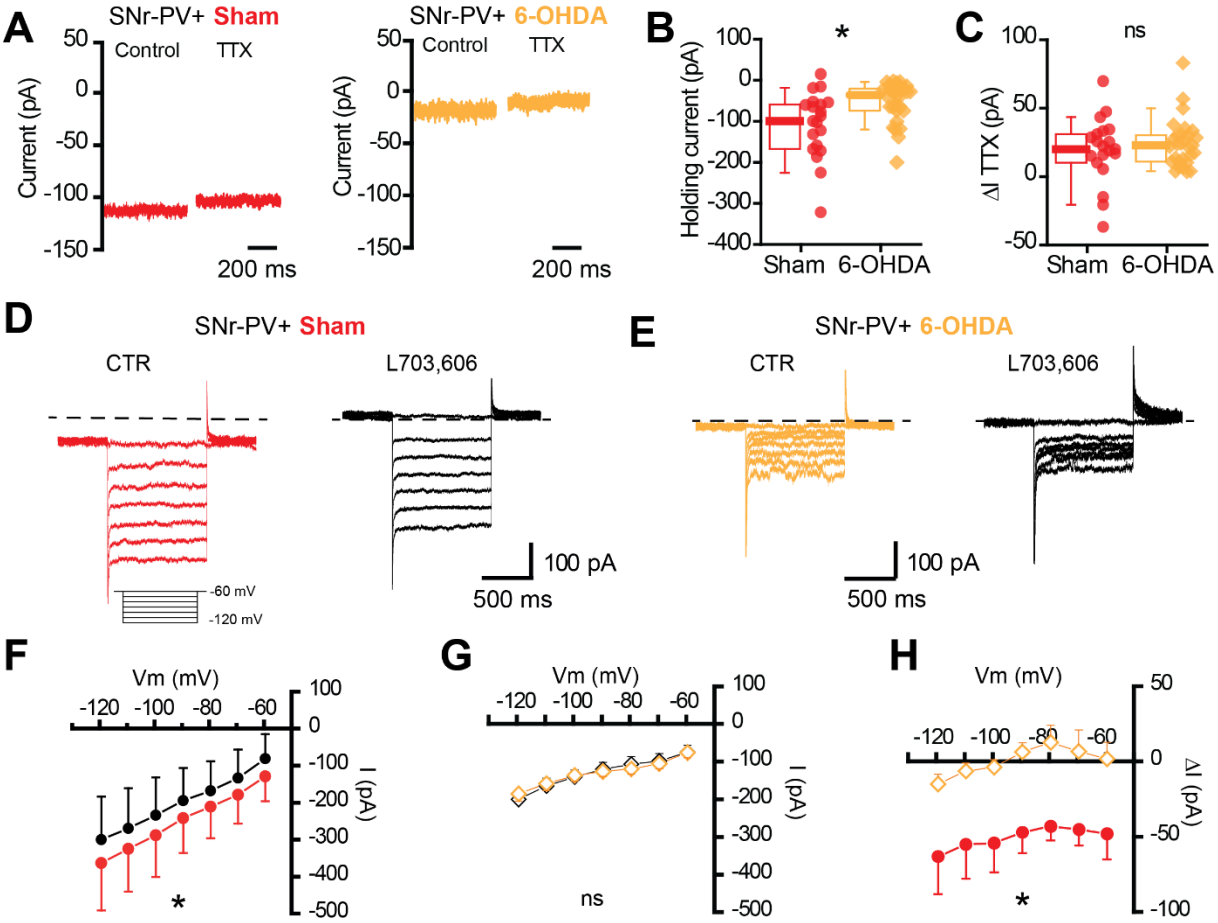

Figure S3: Biophysical properties of NALCN channels on SNr-PV+ neurons in sham and 6-OHDA mice. (Related to figure 4).

A: Representative traces of holding currents recorded at a potential of -60 mV in SNr-PV+ neurons from sham (red) and 6-OHDA (orange) mice before (control) and after bath application of tetrodotoxin (TTX; 1µM) in the ACSF. Note that voltage-dependent sodium channel inhibition by TTX has the same effect on the holding current in sham and 6-OHDA mice. **B:** Population data (sham, n=20; 6-OHDA, n=29) representing a significant increase in the holding current of SN-PV+ cells after the 6-OHDA lesion. **C:** Difference in the holding current by application of 1µM of TTX**. D-E:** Representative curves of SNr-PV+ neurons from sham and 6-OHDA mice to voltage-clamp application of 1s hyperpolarizing steps (holding potential, V_h= -60 mV). The range used was from -120 mV to -60 mV in 10 mV steps. **F:** The current-voltage (I-V) relationship in sham mice (n=7) before (red) and after bath application of L703,606 (10 µM, black). Note a significant reduction of the I-V curve in presence of 10 µM of ZD 7288 to reduce the hyperpolarization-activated current (Ih). **G:** I-V curves of SNr-PV+ neurons from 6-OHDA mice (n=6) before (orange) and after (black) perfusion of L703,606. **H:** Subtraction of I-V curves in sham (C) and 6-OHDA (D) mice. **B-C:** Box-and-whisker plots indicate medians, inter-quartile and 10–90 ranges values. **F-H:** Data are presented as mean ± SEM. *p<0.05, ns: not significant. See Table S3 for more details and statistical information.

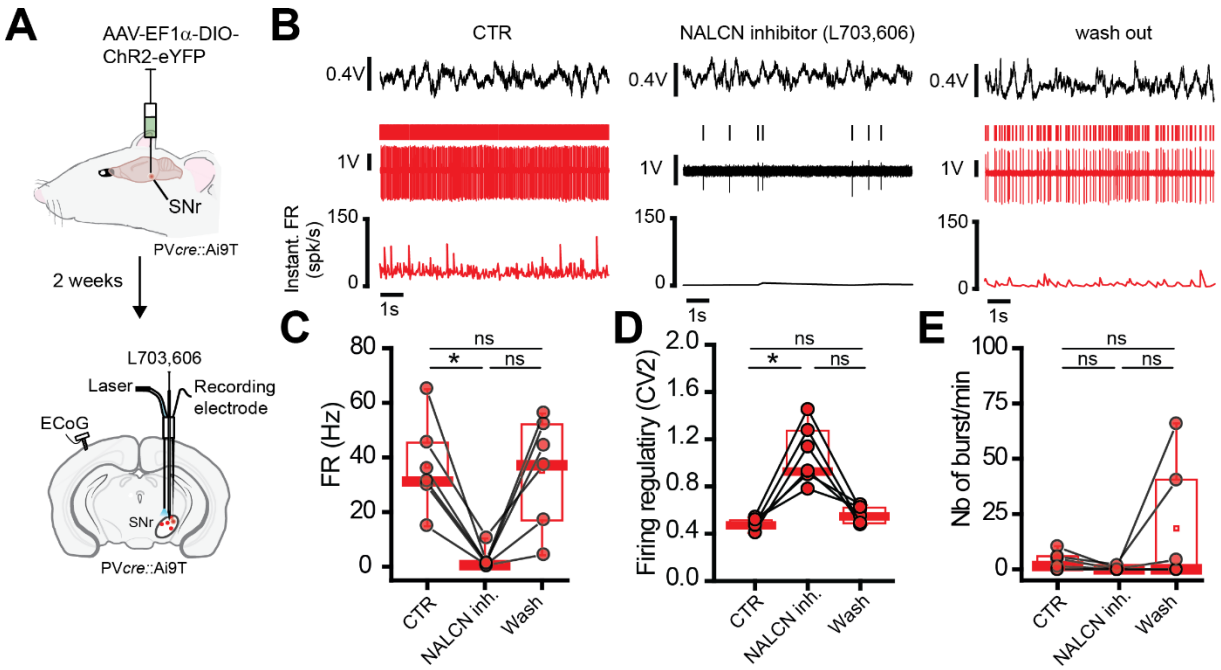

Figure S4: *In vivo* inhibition of NALCN channels reduces the activity of SNr-PV+ neurons in control mice. (Related to figures 4-5).

A: Diagram of the experimental design followed for *in vivo* recordings. The NALCN blocker (L703,606; 50 μM) is applied *via* a cannula placed just above the recording electrode. **B:** Examples traces from a SNr-PV+ neuron recorded before (CTR), during L703,606 local infusion (NALCN inhibitor) and 30 minutes post-injection (wash out). **C:** Mean firing rates of SNr-PV+ neurons from sham (n=3) mice before, during and after NALCN inhibitor locally infused. Note a significant reduction on the FR after blockade of NALCN. **D-E:** Population data showing the effect of NALCN inhibition on FR (**D**), firing regularity (**E**) and the number of burst/min (**F**) on SNr-PV+ cells from control mice. Box-and-whisker plots indicate median, inter- quartile, and 10-90 range values. *p<0.05. See Table S3 for more details and statistical information.

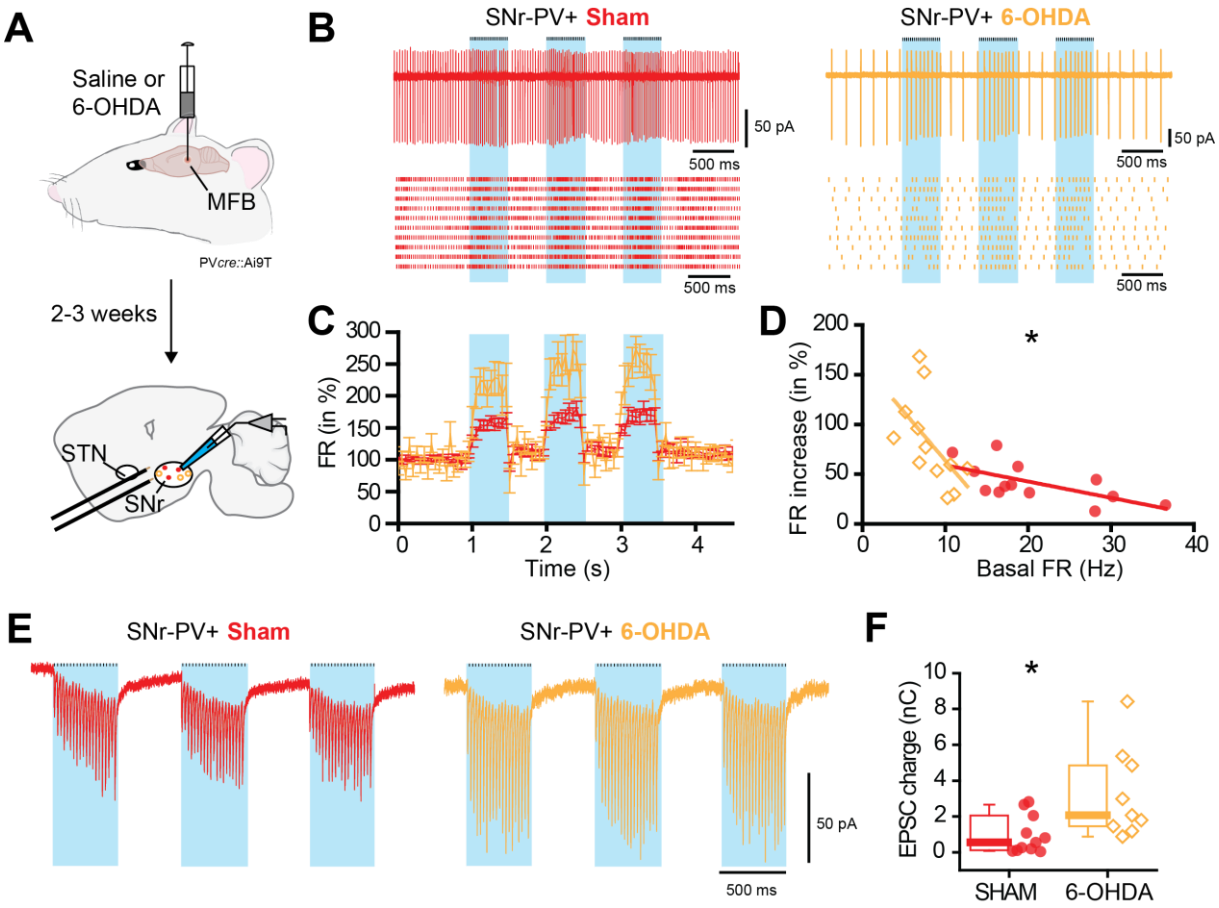

Figure S5. Electrical stimulation of the glutamatergic STN-SNr pathway has a stronger impact on SNr-PV+ firing neurons and elicits bigger synaptic responses under parkinsonian conditions (Related to figure 6).

A: Schematic of the experimental design followed for electrical *ex vivo* experiments. Stimulation electrode is placed between the STN and the SNr and inhibitory transmission is blocked by bath application of CGP 55845 (1 μM) and GABAzine (10μM). **B:** Example traces and raster plots of SNr-PV+ neurons from sham (red) and 6-OHDA (orange) mice during 3 trains of 20 electrical stimulations. **C:** Normalized increase in firing rate (FR) for all recorded SNr-PV+ cells in sham and 6-OHDA mice. **D:** Graph representing the increase in FR (in %) in function of the basal firing of SNr-PV+ neurons. The lines represent the linear regression of the dataset for SNr-PV+ cells from sham (n=13) and 6-OHDA (n=12) mice, respectively. **E:** Examples of synaptic responses recorded in whole-cell configuration using the same stimulation protocol. **F:** Box plots representing the charge of the excitatory postsynaptic currents (EPSC) in both conditions. Note the significant increase in the EPSC train charge after in DA-depleted mice. In C data are presented as Mean ± S.E.M. Box-and-whisker plots indicate median, inter- quartile, and 10-90 range values. *p<0.05. See Table S3 for more details and statistical information.

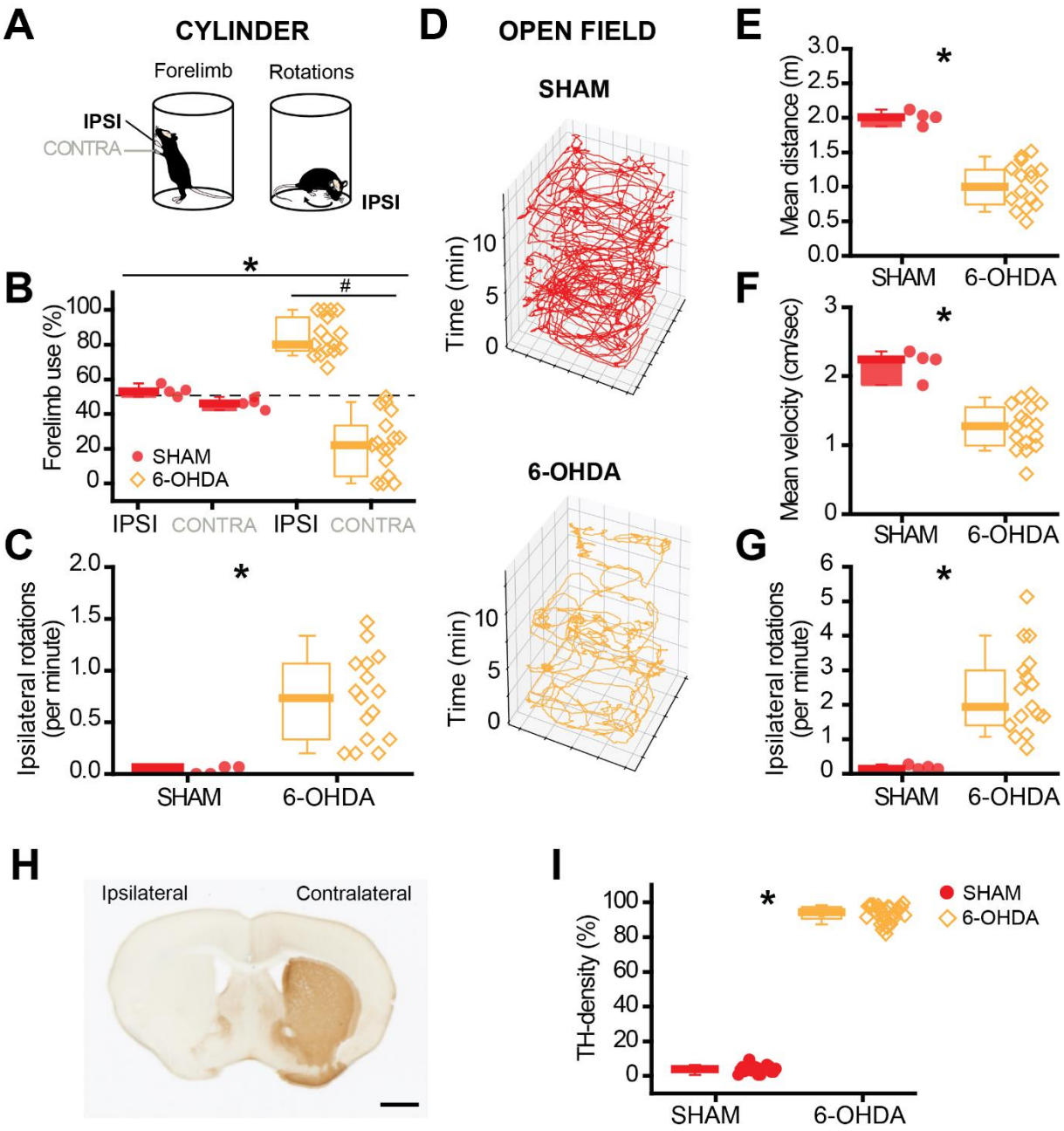

Figure S6: Motor performance of sham and 6-OHDA mice in the cylinder and open field tests along with immunohistochemical validation of the DA depletion (Related to STAR methods and figure 7).

A: Schematic of the different parameters examined in the cylinder test in sham (4 mice) and 6-OHDA (16 mice) mice. **B**: Forelimb use on the wall of the cylinder in sham (red) and 6-OHDA (orange) mice. Note symmetry in the use of the ipsilateral (IPSI) and contralateral (CONTRA) forelimbs use in sham mice whereas the percentage of the contralateral forelimb use is dramatically decreased after the 6-OHDA lesion. **C**: Number of ipsilateral rotations in sham and 6-OHDA-induced hemiparkinsonian mice. **D**: Representative distance travelled in the open field in sham and 6-OHDA mice over 15 min. **E-G**: Average mean distance (**E**), mean velocity (**F**) and number of ipsilateral rotations (**G**) in sham and 6-OHDA mice. **H:** TH-immunostaining in the STR of 300-µm thick coronal sections of a DA depleted mouse. Note the total absence of staining in the ipsilateral site to the 6-OHDA injection. Scale bar: 1mm. **I:** Population graph showing the mean percentage value of striatal TH-fiber density reduction in the ipsilateral site to the lesion from sham (red; 18 mice) and 6-OHDA (orange; 31 mice) mice. Box-and-whisker plots indicate median, first and third quartile, 10-90 range values. * $p<0.05$,

2-way ANOVA; # $p<0.05$, Sidak's post hoc test, See Table S3 for more details and statistical information.

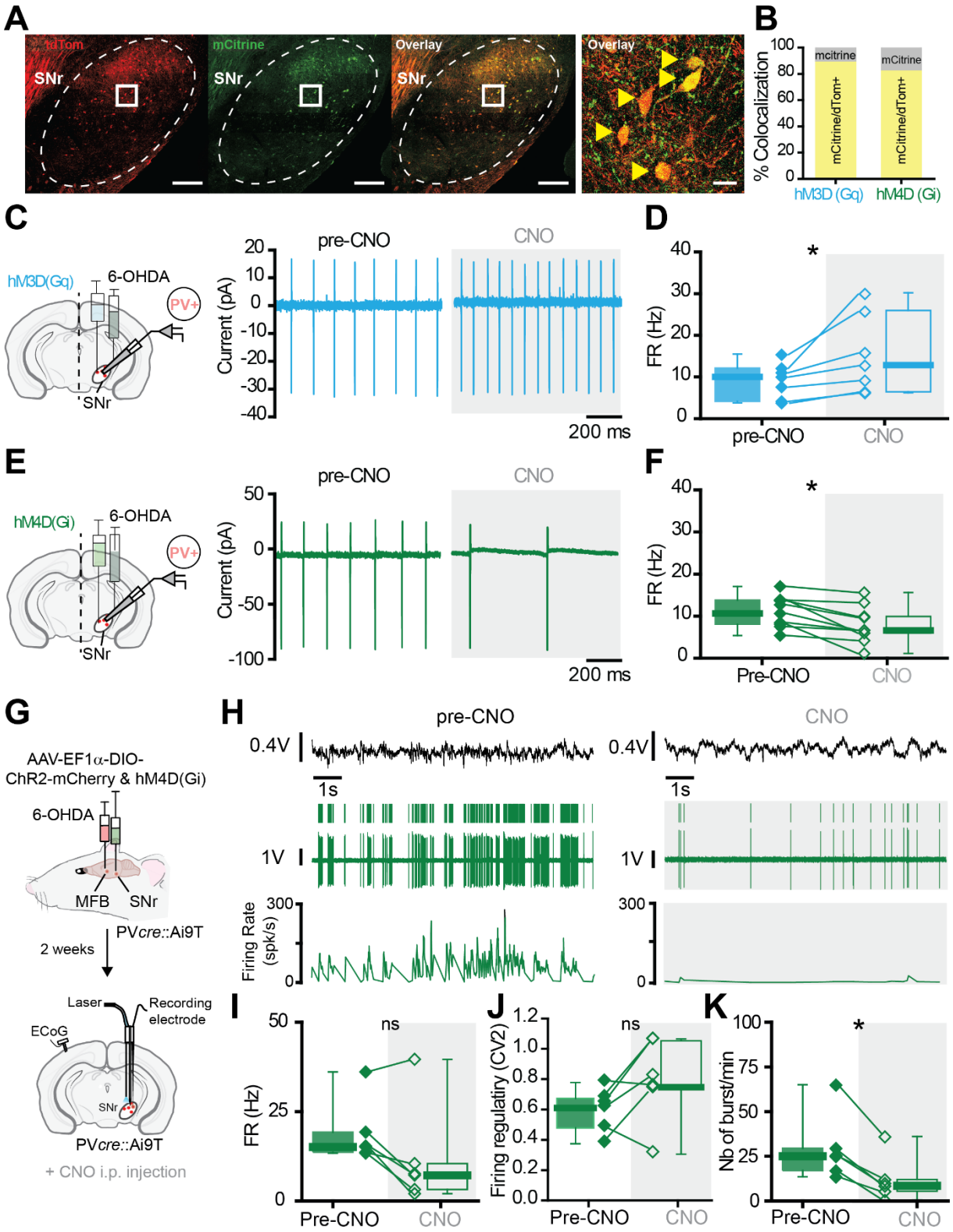

Supplemental figure 7: Validation of the DREADD strategy to manipulate the activity of SNr-PV+ neurons. (Related to Figure 7).

A: *Left*, low-magnification confocal images to validate DREADDs expression (mCitrine in green) faithfully in SNr-PV+ cells (red). Scale bar: 200µm. *Right*, high-magnification image depicting the co-localization between tdTomato and mCitrine (white arrowheads). Scale bar: 30 µm. **B:** Quantification of the percentage of double tdTomato+ and mCitrine+ neurons in 4 mice expressing Gq and 4 mice expressing Gi DREADDs. **C-D:** Representative diagram, traces (C) and population data (D) showing that administration of 10 µM CNO to slices from hemiparkinsonian mice expressing Gq DREADDs

significantly increased the autonomous activity of SNr-PV+ (n=7) neurons. **E-F:** Perfusion of 10 µM CNO in slices from unilateral 6-OHDA mice expressing DREADDs decreased the autonomous pacemaking of SNr-PV+ (n= 10) neurons. All the experiments were performed in presence of AP5 (50 µM), DNQX (10 µM) and GABAzine (10µM) to selectively block NMDA, AMPA and $GABA_A$ receptors, respectively. **G:** Experimental design followed for *in vivo* recordings from 6-OHDA mice expressing DIO-ChR2 and Gi DREADDs. CNO (2mg/kg) was injected i.p. as for behavioural experiments. **H:** Example recordings of SNr-PV+ neurons from lesioned mice before and 30 minutes after CNO injection. **I:** Population data showing a tendency to reduce their FR after CNO injections. **J:** Graph depicting the firing regularity of these neurons under control and in presence of CNO. **K:** Box plots showing a huge reduction on the number of burst per minute 30 minutes after CNO i.p. injections. Group data represented with box-and-whisker plots indicate median, first and third quartile, min and max values. *p<0.05, ns: not significant. See Table S3 for more details and statistical information.

Table S1. Statistical information. Related to Figure 1

Brain structure	Abbreviation	Nb of mice/Nb of slices	Data Value (mean ± SEM)	Significance level
Ventroanterior thalamus	**ThVa**	3/27	2.56 ± 0.24	
Ventromedial thalamus	**ThVM**	3/27	6.29 ± 0.76	
Mediodorsal thalamus	**ThMD**	3/27	4.26 ± 1.17	
Centro-medial/lateral thalamus	**ThCL/CM**	3/27	2.05 ± 0.53	
Parafascicular	**Pf**	3/27	2.95 ± 1.03	
Posterior triangular	**PoT**	3/27	2.77 ± 0.37	
Ethmoid	**Eth**	3/27	2.36 ± 0.57	
Thalamic reticular	**TR**	3/27	1.34 ± 0.14	
Anterior pretectal nucleus dorsal	**APTP**	3/27	5.01 ± 0.91	
Zona incerta dorsal	**Zid**	3/27	3.56 ± 0.67	
Zona incerta ventral	**Ziv**	3/27	3.42 ± 1.09	
Fields of Forel	**FF**	3/27	3.17 ± 0.89	
Prerubral field	**Pr**	3/27	1.83 ± 0.34	
Lateral superior colliculus	**LSC**	3/27	5.23 ± 1.18	
Central superior colliculus	**CSC**	3/27	3.17 ± 0.48	
Medial superior colliculus	**MSC**	3/27	1.77 ± 0.49	
Inferior colliculus	**IC**	3/27	2.31 ± 0.85	
Pedunculopontine nucleus	**PPN**	3/27	4.97 ± 1.75	
Dorsal raphe	**DR**	3/27	1.45 ± 0.52	
Pontine reticular formation, oralis	**Pno**	3/27	1.34 ± 0.54	
Parvicellcular reticular formation	**PcRt**	3/27	0.59 ± 0.27	
Intermediate reticular formation	**Irt**	3/27	0.51 ± 0.12	NR
Midbrain reticular formation	**MidRF**	3/27	4.34 ± 0.76	
Interstitial nucleus of Cajal	**InC**	3/27	4.04 ± 1.55	
PreEdinger-Westphal	**PrEW**	3/27	0.66 ± 0.29	
Rostral interstitial	**RI**	3/27	1.42 ± 0.31	
Supraoculomotor	**Su3**	3/27	1.83 ± 0.33	
Medial accessory oculomotor	**MA3**	3/27	0.84 ± 0.26	
Lateral periaqueductal gray	**lPAG**	3/27	1.75 ± 0.76	
Dorsolateral periaqueductal gray	**dlPAG**	3/27	1.29 ± 0.59	
Ventrolateral periaqueductal gray	**vlPAG**	3/27	1.68 ± 0.87	
Red nucleus	**RN**	3/27	2.8 ± 0.34	
Pararubral	**PaR**	3/27	4.05 ± 0.82	
Cuneiform	**CnF**	3/27	2.06 ± 0.79	
PreCuneiform	**PrCnF**	3/27	1.61 ± 0.65	
Medial parabrachial	**MBP**	3/27	1.59 ± 0.63	
Lateral parabrachial	**LBP**	3/27	2.99 ± 0.49	
Supratrigeminal	**Su5**	3/27	0.77 ± 0.48	
Peritrigeminal	**P5**	3/27	0.85 ± 0.29	
Lateral trigeminal	**L5**	3/27	1.56 ± 0.77	
Globus pallidus, internal	**GPi**	3/27	0.56 ± 0.21	
Subthalamic nucleus	**STN**	3/27	0.97 ± 0.14	
Substantia nigra compacta	**SNc**	3/27	1.96 ± 0.21	

*NR: not reported

Table S2. Statistical information. Related to Figure 1 to 7

Figure	Parameter	Data Type	Mice # / slices #	Data Value (Mean ± SEM)	Statistical test	Significance level
1B	% of SNr neurons	% tdTom$^+$	6/22	57.55± 1.98	NR	NR
		% tdTom$^-$	6/22	38.97 ± 1.92		
		% TH	6/22	3.49 ± 0.36		
1D	% of SNr neurons per level	Rostral/tdTom$^+$	6/22	53.73 ± 2.63	2way ANOVA	Interaction: F (4, 30) = 0.5865 P=0.6749
		Rostral/tdTom$^-$	6/22	42.97 ± 3.59		
		Rostral/TH	6/22	3.3 ± 3.81		
		Central/tdTom$^+$	6/22	48.45 ± 0.78		
		Central/tdTom$^-$	6/22	47.06 ± 8.60		
		Central/TH	6/22	4.49 ± 1.01		
		Caudal/tdTom$^+$	6/22	52.42 ± 2.48		
		Caudal/tdTom$^-$	6/22	43.95 ± 3.38		
		Caudal/TH	6/22	3.63 ± 3.21		
1E	% of SNr neurons per region	DL/tdTom$^+$	6/6	59.87 ± 2.21	2way ANOVA	Interaction: F (2, 20) = 31.84 P<0.0001 Sidak's post hoc: DL: P<0.0001 VM: P<0.0001
		DL/tdTom$^-$	6/6	34.20 ± 1.38		
		DL/TH	6/6	5.93 ± 1.81		
		VM/tdTom$^+$	6/6	33.63 ± 4.22		
		VM/tdTom$^-$	6/6	59.45 ± 2.64		
		VM/TH	6/6	6.92 ± 2.60		
Figure	**Parameter**	**Data Type**	**Mice # / slices #**	**Data Value** (MEDIAN ± M.A.D)	**Statistical test**	**Significance level**
2C	Firing rate, FR (Hz)	PV+	5/18	25.8 ± 5.17	Mann-Whitney U test	U=0 P<0.0001
		PV-	7/14	9.52 ± 2.48		
	Firing regularity (CV2)	PV+	5/18	0.086 ± 0.03	Mann-Whitney U test	U=118 P=0.7788
		PV-	7/14	0.090 ± 0.02		
2E	Membrane potential, Vm (mV)	PV+	3/12	-45.73 ± 3.93	Mann-Whitney U test	U=20 P=0.0148
		PV-	3/9	-56.33 ± 6.77		
	Membrane resistance, Rm (GΩ)	PV+	3/11	0.29 ± 0.14	Mann-Whitney U test	U=11 P=0.0050
		PV-	3/8	0.63 ± 0.21		
	Membrane capacitance, Cm (pF)	PV+	3/11	162.33 ± 52.15	Mann-Whitney U test	U=12 P=0.0068
		PV-	3/8	104.16 ± 27.43		
2G	Action potential threshold, APth (mV)	PV+	3/12	-33.45 ± 4.27	Mann-Whitney U test	U=20.5, P=0.0156
		PV-	3/9	-45.21 ± 5.17		
	Action potential height (mV)	PV+	3/12	62.4 ± 8.11	Mann-Whitney U test	U=36, P=0.2188
		PV-	3/9	69.8 ± 8.8		
	Action potential ½ width (ms)	PV+	3/12	0.58 ± 0.13	Mann-Whitney U test	U=30, P=0.0912
		PV-	3/9	0.52 ± 0.07		
2I, Left	F-I curve (spks/s)	PV+	3/13	NR	Mann-Whitney U test	U=199.5, P=0.9945
		PV-	3/9	NR		
2I, Right	FR gain	PV+	3/13	6.40 ± 2.36	Mann-Whitney U test	U=9, P=0.0004
		PV-	3/9	16.33 ± 3.88		
2K	Rebound FR Max (Hz)	PV+	3/12	52.41 ± 26.97	Mann-Whitney U tes	U=20, P=0.0148
		PV-	3/9	18.21 ± 10.11		
2L	1st AP latency (ms)	PV+	3/12	80.82 ± 21.86	Mann-Whitney U tes	U=20, P=0.0148
		PV-	3/9	108.9 ± 43		
3C	Firing rate, FR (Hz)	PV+_Sham	5/18	25.80 ± 5.17	2way ANOVA	Interaction: F (1, 61) = 31.93 P<0.0001 Sidak's post hoc: P<0.0001 PV+_Sham vs PV-_Sham PV+_Sham vs PV+_6-OHDA
		PV+_6-OHDA	6/19	8.07 ± 3.14		
		PV-_Sham	7/14	9.52 ± 2.48		
		PV-_6-OHDA	6/14	5.74 ± 3.54		

						PV+_Sham vs PV-_6-OHDA
3D	Firing regularity (CV2)	PV+_Sham	5/18	0.098 ± 0.01	2way ANOVA	Interaction: F (1, 61) = 1.487 P=0.2274
		PV+_6-OHDA	6/19	0.12 ± 0.01		
		PV-_Sham	7/14	0.09 ± 0.01		
		PV-_6-OHDA	6/14	0.16 ± 0.02		
4B	Membrane capacitance, Cm (pF)	PV+_Sham	3/11	162.33 ± 52.15	Mann-Whitney U test	U=4, P<0.0001
		PV+_6-OHDA	3/11	82.35 ± 27.95		
4C	Volume (μm^3)	PV+_Sham	3/14	2083.56 ± 1168.93	Mann-Whitney U test	U=45, P=0.0079
		PV+_6-OHDA	4/15	1308.55 ± 455.65		
4D	Membrane resistance, Rm (GΩ)	PV+_Sham	3/11	0.294 ± 0.145	Mann-Whitney U test	U=0, P<0.0001
		PV+_6-OHDA	3/11	1.04 ± 0.168		
4F	Membrane potential, Vm (mV)	PV+_Sham	3/13	-45.26 ± 4.17	Mann-Whitney U test	U=4, P<0.0001
		PV+_6-OHDA	2/7	-52.73 ± 3.85		
4H	Current difference (I□)- **NMDG**	PV+_Sham □ NMDG	3/6	267.62 ± 29.0	Mann-Whitney U test	P=0.0004
		PV+_6-OHDA □ NMDG	3/9	103.93 ± 15.40		
4J	Current difference (I□)- **Pyr3**	PV+_Sham □ Pyr3	3/7	20.27 ± 7.97	Mann-Whitney U test	P=0.6943
		PV+_6-OHDA □ Pyr3	3/8	14.30 ± 12.96		
4L	Current difference (I□)- **L-703.606**	PV+_Sham □ L703.606	4/7	96.36 ± 34.18	Mann-Whitney U test	P<0.0001
		PV+_6-OHDA □ L703.606	4/15	13.89 ± 6.00		
5F	Firing rate, FR (Hz)	PV+_Sham	5/29	21.43 ± 11.53	Mann-Whitney U test	U=311, P=0.6877
		PV+_6-OHDA	5/23	20.01 ± 11.86		
5G	Firing regularity (CV2)	PV+_Sham	5/29	0.50 ± 0.08	Mann-Whitney U test	U=292, P=0.4533
		PV+_6-OHDA	5/23	0.51 ± 0.12		
5H	Mean Inst. FR (spks/s)	PV+_Sham	5/29	27.80 ± 17.33	Mann-Whitney U test	U=185, P=0.0056
		PV+_6-OHDA	5/23	58.38 ± 26.02		
5I	Time in pause (%)	PV+_Sham	5/29	17.44 ± 9.76	Mann-Whitney U test	U=120, P<0.0001
		PV+_6-OHDA	5/23	50.22 ± 16.73		
5J	Mean pause duration (s)	PV+_Sham	5/29	0.26 ± 0.38	Mann-Whitney U test	U=289, P=0.0185
		PV+_6-OHDA	5/23	0.44 ± 0.81		
5K	Nb of burst/min	PV+_Sham	5/29	5.77 ± 4.33	Mann-Whitney U test	U=67, P<0.0001
		PV+_6-OHDA	5/23	32.01 ± 17.21		
5L	% spike in burst	PV+_Sham	5/29	30.94 ± 16.65	Mann-Whitney U test	U=68, P<0.0001
		PV+_6-OHDA	5/23	74.12 ± 14.95		
6D	Mean FR (Hz) PV+_SHAM	CTR	2/7	23.31 ± 9.79	Friedman test	F=7.714, P=0.0207 Dunn's test: CTR vs Glu; P=0.0485 Glu vs Wash; P=0.0485
		Glu		13.81 ± 10.44		
		Wash		24.78 ± 14.17		
	Mean FR (Hz) PV+_6-OHDA	CTR	5/13	31.84 ± 19.36	Friedman test	F=20.46, P<0.0001 Dunn's test: CTR vs Glu; P<0.0001 Glu vs Wash out; P=0.0026
		Glu		10.62 ± 8.04		
		Wash		26.68 ± 13.49		
6E	Mean Inst FR PV+_SHAM	CTR	2/7	36.27 ± 13.32	Friedman test	F= 5.429, P=0.0854
		Glu		31.64 ± 10.59		
		Wash		37.05 ± 14.90		
	Mean Inst FR	CTR	5/13	106.54 ± 32.72		F= 22.5,

	PV+_6-OHDA	Glu		55.6 ± 21.4	Friedman test	P<0.0001 Dunn's test: CTR vs Glu; P<0.0001
		Wash		79.32 ± 26.75		
6F	Time in pause (%) PV+_SHAM	CTR	2/7	6.44 ± 9.01	Friedman test	F= 2.000, P=0.4861
		Glu		34.51 ± 24.73		
		Wash		3.58 ± 10.56		
	Time in pause (%) PV+_6-OHDA	CTR	5/13	47.91 ± 19.96	Friedman test	F= 17.23, P=0.0002 Dunn's test: CTR vs Glu; P=0.0003 Glu vs Wash out; P=0.0051
		Glu		83.97 ± 14		
		Wash		55.58 ± 18.73		
6G	Mean pause (s) PV+_SHAM	CTR	2/7	0.21 ± 0.21	Friedman test	F= 4.571, P=0.1118
		Glu		0.46 ± 0.46		
		Wash		0.12 ± 0.20		
	Mean pause (s) PV+_6-OHDA	CTR	5/13	0.27 ± 0.14	Friedman test	F= 17.08, P=0.0002 Dunn's test: CTR vs Glu; P=0.0001
		Glu		0.45 ± 0.36		
		Wash		0.26 ± 0.15		
6H	Nb of burst/min PV+_SHAM	CTR	2/7	9.00 ± 5.73	Friedman test	F= 6.889, P=0.0249 Dunn's test: Glu vs Wash out; P=0.0485
		Glu		6.00 ± 2.98		
		Wash		9.5 ± 6.16		
	Nb of burst/min PV+_6-OHDA	CTR	5/13	80.0 ± 28.0	Friedman test	F= 17.74, P=0.0001 Dunn's test: CTR vs Glu; P=0.0004 Glu vs Wash out; P=0.0098
		Glu		3.00 ± 20.87		
		Wash		48.00 ± 30.45		
6I	% spike in burst PV+_SHAM	CTR	2/7	27.3 ± 10.42	Friedman test	F= 5.429, P=0.0854
		Glu		17.53 ± 8.81		
		Wash		24.95 ± 26.9		
	% spike in burst PV+_6-OHDA	CTR	5/13	72.85 ± 22.13	Friedman test	F= 12.38, P=0.0020 Dunn's test: CTR vs Glu; P=0.0036
		Glu		4.74 ± 30.81		
		Wash		55.74 ± 25.1		

Figure	**Parameter**	**Data Type**	**Mice # / slices #**	**Data Value (Mean ± SEM)**	**Statistical test**	**Significance level**
7C	Forelimb use (%) CONTRA	EF1a-eYFP_NaCl	5	18.28 ± 6.44	2way ANOVA	Interaction : F (2, 13) = 16.26 P=0.0003 Sidak's post hoc: P<0.0001 hM4D(Gi) NaCl vs CNO
		EF1a-eYFP_CNO		25.13 ± 6.73		
		hM3D(Gq)_NaCl	4	20.9 ± 6.21		
		hM3D(Gq)_CNO		13.4 ± 7.77		
		hM4D(Gi)_NaCl	7	12.2 ± 4.57		
		hM4D(Gi)_CNO		40.08 ± 2.35		
7D	Ipsilateral rotations per min	EF1a-eYFP_NaCl	5	0.55 ± 0.19	2way ANOVA	Interaction : F (2, 13) = 6.3 P=0.0122 Sidak's post hoc: P=0.0014 hM4D(Gi) NaCl vs CNO
		EF1a-eYFP_CNO		0.63 ± 0.26		
		hM3D(Gq)_NaCl	4	0.6 ± 0.2		
		hM3D(Gq)_CNO		0.5 ± 0.10		
		hM4D(Gi)_NaCl	7	0.94 ± 0.14		
		hM4D(Gi)_CNO		0.27 ± 0.06		
7F	Mean distance (m)	EF1a-eYFP_NaCl	5	1.16 ± 0.09	2way ANOVA	Interaction : F (2, 13) = 9.548 P=0.0028 Sidak's post hoc: P=0.0012 hM4D(Gi) NaCl vs CNO
		EF1a-eYFP_CNO		1.18 ± 0.07		
		hM3D(Gq)_NaCl	4	1.05 ± 0.22		
		hM3D(Gq)_CNO		0.87 ± 0.17		
		hM4D(Gi)_NaCl	7	0.93 ± 0.11		
		hM4D(Gi)_CNO		1.31 ± 0.10		
7G	Mean velocity (cm/sec)	EF1a-eYFP_NaCl	5	1.37 ± 0.14	2way ANOVA	Interaction : F (2, 13) = 9.734 P=0.0026 Sidak's post hoc: P=0.0023 hM4D(Gi) NaCl vs CNO
		EF1a-eYFP_CNO		1.34 ± 0.08		
		hM3D(Gq)_NaCl	4	1.18 ± 0.23		
		hM3D(Gq)_CNO		0.98 ± 0.19		
		hM4D(Gi)_NaCl	7	1.24 ± 0.10		
		hM4D(Gi)_CNO		1.60 ± 0.14		
7H	Ipsilateral rotations per min	EF1a-eYFP_NaCl	5	1.95 ± 0.49	2way ANOVA	Interaction : F (2, 13) = 10.66 P=0.0018 Sidak's post hoc: P=0.0011 hM4D(Gi) NaCl vs CNO
		EF1a-eYFP_CNO		2.2 ± 0.57		
		hM3D(Gq)_NaCl	4	1.53 ± 0.19		
		hM3D(Gq)_CNO		2.3 ± 0.39		
		hM4D(Gi)_NaCl	7	3.24 ± 0.45		
		hM4D(Gi)_CNO		1.47 ± 0.35		

Table S3. Statistical information. Related to supplemental Figure S1 to S7

Figure	Parameter	Data Type	Nb of mice/Nb of slices	Data Value (mean ± SEM)	Statistical test	Significance level
S1B	% co-localization tdTom/PV	% dTom/PV	6/13	75.7 ± 2.84	NR	NR
		% dTom	6/13	13.12 ± 2.83		
		% PV	6/13	11.8 ± 2.04		
Figure	**Parameter**	**Data Type**	**Nb of mice/Nb of neurons**	**Data Value** (MEDIAN ± M.A.D)	**Statistical test**	**Significance level**
S2C	Holding current (pA)	PV+_Sham	3/6	-179.02 ± 49.43	Mann-Whitney U test	U=0, p=0.0043
		PV-_Sham	3/5	-42.25 ± 9.03		
S2D	Current difference (ΔI)- **TTX** (pA)	PV+_Sham	3/6	3.77 ± 25.59	Whitney U test	U=15, P>0.9999
		PV-_Sham	3/5	-1.92 ± 9.13		
S2E	Current difference (ΔI)- **NMDG** (pA)	PV+_Sham	3/6	267.62 ± 30.00	Mann-Whitney U test	U=0, P=0.0043
		PV-_Sham	3/5	59.18 ± 11.39		
S3B	Holding Current (pA)	PV+_Sham	10/20	-93.1 ± 62.10	Mann-Whitney U test	U=160, P=0.0075
		PV+_6-OHDA	10/29	-36 ± 38.29		
S3C	Current difference (ΔI)- **TTX** (pA)	PV+_Sham	10/20	21.27 ± 16.59	Mann-Whitney U test	U=281, P=0.8640
		PV+_6-OHDA	10/29	22.76 ± 12.43		
S3F	I-V curve (pA)	PV+_Sham	3/7	NR	Wilcoxon signed rank test	P=0.0156
S3G	I-V curve (pA)	PV+_6-OHDA	3/9	NR	Wilcoxon signed rank test	P=0.9375
S3H	Δ I-V curve (pA)	PV+_sham Vs PV+_6-OHDA	3/7 3/9	NR	Mann-Whitney U test	U=0, P=0.0006
S4C	Mean FR (Hz) PV+_SHAM	CTR	3/6	33.52 ± 10.09	Friedman test	F=9.33, P=0.0055 Dunn's test: P=0.0117 CTR vs NALCN inh
		NALCN inh.		0.86 ± 2.68		
		Wash		40.73 ± 16.37		
S4D	Firing regularity (CV2)	CTR	3/6	0.48 ± 0.03	Friedman test	F=12, P=0.0001 Dunn's test: P=0.0117 CTR vs NALCN inh
		NALCN inh.		1.03 ± 0.21		
		Wash		0.57 ± 0.06		
S4E	Nb of burst/min PV+_SHAM	CTR	3/6	3.25 ± 3.33	Friedman test	F=5.20, P=0.0741
		NALCN inh.		0. 00 ± 0.55		
		Wash		2.25 ± 23.13		
S5D	FR increase (%)	PV+_Sham	4/13	37.64 ± 15.15	Linear regression	F=5.388 P=0.0304
		PV+_6-OHDA	3/12	69.25 ± 34.68		
S5F	EPSC charge (nC)	PV+_Sham	4/11	0.56 ± 0.861		U=15, P=0.0074

		PV+_6-OHDA	3/9	2.06 ± 1.99	Mann-Whitney U test	
S6B	Forelimb use (%)	IPSI_Sham	4	53.44 ± 2.17	2way ANOVA	Interaction : F (1, 18) =18.68 P=0.004 Sidak's post hoc: P<0.0001 6-OHDA: IPSI vs CONTRA
		IPSI_6-OHDA	16	81.66 ± 9.44		
		CONTRA_Sham	4	46.56 ± 2.17		
		CONTRA_6-OHDA	16	22.87 ± 13.43		
S6C	Ipsilateral rotations per min	Sham	4	0.03 ± 0.03	Mann-Whitney U test	U=0, P=0.0002
		6-OHDA	16	0.76 ± 0.34		
S6E	Mean distance (m)	Sham	4	2.02 ± 0.06	Mann-Whitney U test	U=0, P=0.0004
		6-OHDA	16	1.07 ± 0.26		
S6F	Mean velocity (cm/sec)	Sham	4	2.25 ± 0.15	Mann-Whitney U test	U=0, P=0.004
		6-OHDA	16	1.28 ± 0.26		
S6G	Ipsilateral rotations per min	Sham	4	0.16 ± 0.05	Mann-Whitney U test	U=0, P=0.0004
		6-OHDA	16	2.2 ± 0.99		
S6I	TH-density (%)	SHAM	18	4.08 ±1.63	Mann-Whitney U test	U=0, P<0.0001
		6-OHDA	31	94.41 ± 3.86		
S7B	% Colocalization	hM3D (Gq)	4	88.5 ± 3.75	NR	NR
		hM4D (Gi)	4	84.74 ± 4.56	NR	NR
S7D	Firing rate (FR) hM3D (Gq)	Pre CNO	2/7	9.96 ± 3.39	Wilcoxon signed rank test	P=0.0156
		CNO		12.71 ± 7.44		
S7F	Firing rate (FR) hM4D (Gi)	Pre CNO	5/10	11.65 ± 3.31	Wilcoxon signed rank test	P=0.0020
		CNO		7.35 ± 3.14		
S7I	Firing rate in vivo (FR) hM4D (Gi)	Pre CNO	6	15.22 ± 5.91	Wilcoxon signed rank test	P=0.0938
		CNO		7.04 ± 9.30		
S7J	CV2 hM4D (Gi)	Pre CNO	6	0.62 ± 0.11	Wilcoxon signed rank test	P=0.1563
		CNO		0.78 ± 0.19		
S7K	Nb of burst/min hM4D (Gi)	Pre CNO	6	25.25 ± 12	Wilcoxon signed rank test	P=0.0313
		CNO		9.25 ± 7.97		